


RESEARCH ARTICLE

Modeling longitudinal imaging biomarkers with parametric Bayesian multi-task learning

Leon M. Aksman¹  | Marzia A. Scelsi¹ | Andre F. Marquand² | Daniel C. Alexander¹ | Sebastien Ourselin^{1,3} | Andre Altmann¹ | for ADNI[†]

¹Centre for Medical Image Computing, University College London, London, UK

²Donders Centre for Cognitive Neuroimaging, Donders Institute for Brain, Cognition and Behaviour, Radboud University, Nijmegen, The Netherlands

³School of Biomedical Engineering and Imaging Sciences, St Thomas' Hospital, King's College London, London, UK

Correspondence

Leon M. Aksman, 8th floor, Malet Place Engineering Building, 2 Malet Place, London, WC1E 7JE, UK.

Email: l.aksman@ucl.ac.uk

Funding information

Engineering and Physical Sciences Research Council, Grant/Award Numbers: EP/H046410/1, EP/J020990/1, EP/K005278, EP/L016478/1, J020990, M006093, M020533; FP7 Information and Communication Technologies, Grant/Award Number: FP7-ICT-2011-9-601055; Horizon 2020 Framework Programme, Grant/Award Number: 666992; Medical Research Council, Grant/Award Numbers: MR/J01107X/1, MR/L016311/1; National Institute for Health Research, Grant/Award Number: BW.mn. BRC10269; Nederlandse Organisatie voor Wetenschappelijk Onderzoek, Grant/Award Number: 91716415

Abstract

Longitudinal imaging biomarkers are invaluable for understanding the course of neurodegeneration, promising the ability to track disease progression and to detect disease earlier than cross-sectional biomarkers. To properly realize their potential, biomarker trajectory models must be robust to both under-sampling and measurement errors and should be able to integrate multi-modal information to improve trajectory inference and prediction. Here we present a parametric Bayesian multi-task learning based approach to modeling univariate trajectories across subjects that addresses these criteria. Our approach learns multiple subjects' trajectories within a single model that allows for different types of information sharing, that is, *coupling*, across subjects. It optimizes a combination of uncoupled, fully coupled and kernel coupled models. Kernel-based coupling allows linking subjects' trajectories based on one or more biomarker measures. We demonstrate this using Alzheimer's Disease Neuroimaging Initiative (ADNI) data, where we model longitudinal trajectories of MRI-derived cortical volumes in neurodegeneration, with coupling based on APOE genotype, cerebrospinal fluid (CSF) and amyloid PET-based biomarkers. In addition to detecting established disease effects, we detect disease related changes within the insula that have not received much attention within the literature. Due to its sensitivity in detecting disease effects, its competitive predictive performance and its ability to learn the optimal parameter covariance from data rather than choosing a specific set of random and fixed effects *a priori*, we propose that our model can be used in place of or in addition to linear mixed effects models when modeling biomarker trajectories. A software implementation of the method is publicly available.

KEYWORDS

Alzheimer's disease, Bayesian analysis, biomarkers, longitudinal analysis, machine learning, multimodal analysis, structural MRI

[†]Data used in preparation of this article were obtained from the Alzheimer's Disease Neuroimaging Initiative (ADNI) database (adni.loni.usc.edu). As such, the investigators within the ADNI contributed to the design and implementation of ADNI and/or provided data but did not participate in analysis or writing of this report. A complete listing of ADNI investigators can be found at: http://adni.loni.usc.edu/wp-content/uploads/how_to_apply/ADNI_Acknowledgement_List.pdf.

1 | INTRODUCTION

Despite their value in characterizing the course of neurodegeneration (Freeborough & Fox, 1997; Smith, De Stefano, Jenkinson, &

This is an open access article under the terms of the Creative Commons Attribution License, which permits use, distribution and reproduction in any medium, provided the original work is properly cited.

© 2019 The Authors. *Human Brain Mapping* published by Wiley Periodicals, Inc.

Matthews, 2001), repeated measures over time (i.e., longitudinal data) in neuroimaging are often limited to a baseline measurement and a few follow-up time-points per subject. This is primarily due to the costs and complexities of collecting such data. Consequently, within-subject trajectory models of regions of interest (ROIs) or clinical measures that are based on such limited data may not be robust to measurement errors from image acquisition or post-processing. Such noise may lead to poor inferences of true underlying trajectory parameters and poor predictions of future values, diminishing the value of trajectory based biomarkers (Curran, Obeidat, & Losardo, 2010). An additional problem is a limit to the flexibility of the models that can be estimated: with two time-points one can only estimate a linear model, with three only a quadratic, and so on.

There has been growing interest in methods that efficiently use longitudinal neuroimaging data; e.g., Telzer et al., (Telzer et al., 2018) provide an overview related to fMRI analysis. By far the most popular approaches are based on mixed effect modeling, which combines fixed effects, that is, pooling subjects' data to create an average trajectory for all subjects, with random effects, that is, individualizing models about the average trajectory. The mixed effects modeling approach is well suited to both balanced (fixed number of samples, fixed time interval between samples) and unbalanced (varying samples or time intervals) longitudinal designs, allowing for separate analysis of between and within subject variability (Fitzmaurice, Laird, & Ware, 2011; Laird & Ware, 1982). Bernal-Rusiel et al. (2013) and Guillaume, Hua, Thompson, Waldorp, and Nichols (2014) provide overviews of linear mixed effects (LME) models within neuroimaging and apply them to Alzheimer's disease (AD).

Features from longitudinal measurements remove inter-individual differences and thus make for better descriptions of disease progression. Recent models of disease progression have integrated both cross-sectional and longitudinal information to estimate discrete or continuous disease stages for individuals (Donohue et al., 2014; Fonteijn et al., 2012; Jedynak et al., 2012; Lorenzi et al., 2017; Schiratti, Allasonnière, Colliot, & Durrleman, 2017; Young et al., 2014). They have been inspired by, and seek to quantify the hypothetical models of disease progression proposed by neurodegenerative disease researchers (Buckner et al., 2005; Jack et al., 2010). Oxtoby and Alexander (2017) provide an overview of the methods within this emerging field. While the purpose of disease progression modeling is to estimate disease stage and find group-level (typically monotonic) trajectories for each biomarker, this procedure can be thought of as a form of coupling of biomarker trajectories across subjects. However, most of these models are not explicitly setup to couple subjects' trajectories within each biomarker (e.g., a brain structural ROI) based on other biomarkers' information (e.g., genetic risk or brain amyloid deposition). As such these models may not fully capitalize on valuable multi-modal information that may improve trajectory estimates within each biomarker.

Multi-kernel learning (MKL) presents an approach to combining multiple biomarker similarity measures. It has been previously applied to neuroimage-based pattern recognition and machine learning to discriminate disease (Hinrichs, Singh, Xu, & Johnson, 2011; Zhang, Wang, Zhou, Yuan, & Shen, 2011). Young et al. (2013) applied a Bayesian MKL approach to AD discrimination, which avoided the need for

costly cross-validation when tuning the kernel weightings. In addition to a more efficient means of tuning such hyperparameters, Bayesian modeling also provides a principled approach to incorporating prior information, comparing models, making probabilistic predictions, and inferring distributions over parameters (Gelman et al., 2013). It has been applied in many contexts within neuroimaging (Woolrich, 2012) and more specifically in both parametric and nonparametric trajectory models (Lorenzi, Ziegler, Alexander, & Ourselin, 2015; Ziegler, Penny, Ridgway, Ourselin, & Friston, 2015).

In this article, we develop an approach that realizes the benefits of MKL within a Bayesian trajectory model rather than a disease classification model. To do so we use multi-task learning, which aims to learn multiple related tasks simultaneously, sharing information across tasks. Bayesian MTL was previously applied in neuroimaging within the context of multi-subject fMRI analysis (Marquand, Brammer, Williams, & Doyle, 2014; Marquand, Brammer, et al. 2014) based on the method proposed by Bonilla et al. (2008). Bayesian MTL has also been applied to imaging genetics via a hierarchical Bayesian model that encourages both individual and group sparsity (Greenlaw, Szefer, Graham, Lesperance, & Nathoo, 2017; Nathoo, Greenlaw, & Lesperance, 2016). Here we set the learning of each subject's biomarker trajectory as a task and apply MTL to share information across subjects. We develop a parametric extension of Marquand et al.'s approach, a joint Bayesian linear regression that allows for full coupling across all subjects along with coupling based on biomarker similarity, so that subjects with similar measures in one biomarker may have more similar trajectories in another. Furthermore, we use MKL to couple trajectories within a biomarker based on an optimal balance of multiple other biomarkers' information. We compare our approach, which learns the optimal parameter covariance from data to standard LME modeling, where the parameter covariance structure depends on the a priori choice of random and fixed effects.

This article (a) contributes a parametric model that learns a separate trajectory for each subject while allowing for information-sharing across subjects and the integration of multi-modal information during model training, resulting in better predictions, and inferences; (b) performs simulations to validate the model and understand its properties; (c) applies the model to clinical neuroimaging data, modeling cortical region of interest (ROI) trajectories in neurodegeneration using various biomarkers for coupling and (d) interprets and discusses the results.

2 | METHODOLOGY

2.1 | Model: Parametric Bayesian MTL

We present a univariate model of the temporal trajectory of a scalar variable (e.g., values of an ROI or a clinical measure) across multiple subjects. We set the learning of each subject's trajectory as a task and use MTL to share information across subjects to better learn all subjects' trajectories as a single, coupled model. Empirical Bayes allows us to automatically tune the degree and type of coupling across subjects using hyperparameters that control the overall covariance structure of the parameters being learned.

We start by specifying a single, large model for all n subjects' trajectories, stacking the longitudinal observations of all subjects into the vector $\mathbf{y} = [\mathbf{y}'_1 \dots \mathbf{y}'_n]'$, where \mathbf{y}_i is an $m_i \times 1$ vector of observations for the i th subject. In total, there are $m = \sum_{i=1}^n m_i$ observations across subjects, so that \mathbf{y} is a $m \times 1$ vector. To model these trajectories, we can fit polynomial functions of time (e.g., age) using the following model structure:

$$\mathbf{y} = \mathbf{X}\mathbf{w} + \boldsymbol{\varepsilon} = \begin{bmatrix} \mathbf{X}_1 & & \\ & \ddots & \\ & & \mathbf{X}_n \end{bmatrix} \begin{bmatrix} \mathbf{w}_1 \\ \vdots \\ \mathbf{w}_n \end{bmatrix} + \boldsymbol{\varepsilon} \quad (1)$$

where the overall design matrix \mathbf{X} is block diagonal for a chosen polynomial model of order p , with zeros in the off-diagonal entries. Defining $d = p + 1$, we have block \mathbf{X}_i as the $m_i \times d$ design matrix for subject i having m_i observations at times t_{i1}, \dots, t_{im_i} :

$$\mathbf{X}_i = \begin{bmatrix} 1 & t_{i1} & \dots & t_{i1}^p \\ 1 & t_{i2} & \dots & t_{i2}^p \\ \vdots & \vdots & \ddots & \vdots \\ 1 & t_{im_i} & \dots & t_{im_i}^p \end{bmatrix} \quad (2)$$

and \mathbf{w} is an $nd \times 1$ vector of parameters across subjects. If we assume additive Gaussian noise $\boldsymbol{\varepsilon} \sim N(\mathbf{0}, \beta^{-1}\mathbf{I}_m)$ we can solve the general linear model (GLM) formed by Equation (1) via ordinary least squares (OLS) regression, finding a set of parameters $\mathbf{w}_1, \dots, \mathbf{w}_n$ that describe the subjects' temporal trajectories. Each \mathbf{w}_i is a $d \times 1$ vector containing the trajectory parameters for subject i . In the case of linear models \mathbf{w}_i is 2×1 and contains an intercept and a slope term.

OLS regression is a simple and widely used means of modeling trajectories models for each subject. However, it assumes an independent model for each subject, thereby ignoring the similarity in other subjects' trajectories that may greatly improve both prediction and parameter inference. Using a Bayesian approach, we propose to overcome this problem by placing a prior probability distribution over these parameters. The form of the prior we propose is:

$$p(\mathbf{w}) = N(\mathbf{0}, \boldsymbol{\Sigma}_{\text{prior}}) \quad (3)$$

$$\boldsymbol{\Sigma}_{\text{prior}} = \alpha_1 \mathbf{I}_{nd} + \sum_{i=1}^d \underbrace{\boldsymbol{\Sigma}_{\text{ci}}}_{\text{inter-subject}} \otimes \underbrace{\mathbf{M}_{\text{ii}}}_{\text{intra-subject}} \quad (4)$$

$$\boldsymbol{\Sigma}_{\text{ci}} = \alpha_{i1} \mathbf{I}_n + \alpha_{i2} \mathbf{1}_n + \sum_{j=1}^k \alpha_{i(j+2)} \mathbf{K}_j \quad (5)$$

where \mathbf{M}_{ii} is defined below and $\boldsymbol{\Sigma}_{\text{prior}}$ is of size $nd \times nd$. The first term in Equation (4), with weight α_1 , allows for a diagonal (i.e., independent)

covariance structure in the parameters¹ and ensures the matrix is positive definite. The second term is a sum of d Kronecker products. When fitting linear models (i.e., polynomial models of degree one, as we will do throughout this article), there are two such products: one for the 0th order parameters (i.e., intercepts), the other for the first order parameters (i.e., slopes or rates of change). In each case, we take the Kronecker product of an inter-subject (coupling) matrix and an intra-subject matrix to form part of the overall covariance matrix. Each $\boldsymbol{\Sigma}_{\text{ci}}$ is an $n \times n$ matrix parameterized to allow for fully independent parameters ($\alpha_{i1} \mathbf{I}_n$ term, where \mathbf{I}_n is an n -dimensional identity matrix), fully coupled parameters ($\alpha_{i2} \mathbf{1}_n$ term, where $\mathbf{1}_n$ is an n -dimensional matrix of ones) and coupling based on the set of k biomarker based kernels (the \mathbf{K}_j 's, each an n -dimensional positive definite matrix). The form of these biomarker kernels is detailed later in this paper. As a result, each $\boldsymbol{\Sigma}_{\text{ci}}$ contains at least $k + 2$ hyperparameters² and overall there are at least $d(k + 2)$ covariance-related hyperparameters. It is important to bear in mind the distinction between the hyperparameters (the α 's) used to control coupling among subjects and the parameters of individuals' trajectory models (the \mathbf{w}_i 's stacked within \mathbf{w}).

The intra-subject matrix \mathbf{M}_{ii} describes how the trajectory parameters within each subject's model are related to each other. We have chosen each \mathbf{M}_{ii} to be a $d \times d$ indicator matrix equal to one on the i th diagonal element and zero elsewhere, so that there is no information sharing between different parameter types (e.g., between intercepts and slopes) within and across subjects. This prior structure allows us to learn the inter-subject coupling separately for each parameter type, giving the model a great deal of flexibility.

Note that simpler parametrizations of the covariance matrix are possible. For instance, choosing $\boldsymbol{\Sigma}_{\text{prior}} = \boldsymbol{\Sigma}_{\text{c}} \otimes \mathbf{I}_d$ with \mathbf{I}_d the $d \times d$ identity matrix and $\boldsymbol{\Sigma}_{\text{c}} = \alpha_1 \mathbf{I}_n + \alpha_2 \mathbf{1}_n$ is closest to the form used in Marquand et al. Using instead $\boldsymbol{\Sigma}_{\text{c}} = \alpha_1 \mathbf{I}_n + \alpha_2 \mathbf{1}_n + \sum_{j=1}^k \alpha_{(j+2)} \mathbf{K}_j$ implements MKL. Both variations use fewer hyperparameters than our proposed parametrization. However, these simpler models tie the coupling of parameters types (e.g., intercepts and slopes) together and as such may be more prone to inducing spurious coupling in one set of parameters while capturing true coupling in another (e.g., spuriously coupling intercepts along with slopes). This may, in turn, lead to the increased false positive group differences in subjects' parameters.

This prior structure differs from that used in hierarchical Bayesian modeling, where individuals' first level parameter prior means are specified as linear combinations of second level parameters that may include covariates and grouping variables that also have prior distributions. In contrast, we assume a zero-mean prior on individuals' parameters and incorporate covariates via kernels within each $\boldsymbol{\Sigma}_{\text{ci}}$. Kernels allow for nonlinear similarity measures between covariates, adding modeling flexibility not present in linear hierarchical models. Hierarchical models, in contrast, offer a well-developed framework for modeling fixed and random effects. The two approaches are not mutually exclusive: it is possible to combine them, though for the sake of simplicity we leave this as a topic for future work.

¹In practice, we include an additional diagonal term $\epsilon \mathbf{I}_{nd}$, with ϵ set to 10^{-6} throughout, that aids numerical stability when inverting $\boldsymbol{\Sigma}_{\text{prior}}$.

²There may be more hyperparameters if the kernels themselves contain tuneable parameters.

Finally, we choose the likelihood term, that is, the data observation model, to resemble the GLM from Equation (1), setting

$$p(\mathbf{y}|\mathbf{X}, \mathbf{w}) = N(\mathbf{y}|\mathbf{X}\mathbf{w}, \beta^{-1}\mathbf{I}_m) \quad (6)$$

with \mathbf{X} and \mathbf{w} defined as before. We allow the model to learn the (inverse) measurement noise level β within the likelihood as an additional hyperparameter. With the prior and likelihood thus specified, we can use Bayes' rule to update our beliefs on the parameter distribution given some observed data (i.e., find the posterior distribution). In this case as we have a Gaussian prior and a Gaussian likelihood the posterior is also Gaussian and has the following closed-form solution (Bishop, 2007):

$$p(\mathbf{w}|\mathbf{X}, \mathbf{y}, \alpha, \beta) = N(\mathbf{w}|\bar{\mathbf{w}}, \Sigma_{\text{post}}) \quad (7)$$

$$\Sigma_{\text{post}} = \left(\Sigma(\alpha)_{\text{prior}}^{-1} + \beta \mathbf{X}^T \mathbf{X} \right)^{-1} \quad (8)$$

$$\bar{\mathbf{w}} = \beta \Sigma_{\text{post}} \mathbf{X}^T \mathbf{y} \quad (9)$$

where we have collected the covariance prior's hyperparameters into the vector α and have made the dependence of the prior covariance on these parameters explicit using the notation $\Sigma(\alpha)_{\text{prior}}$.

To estimate optimal values for α and β , we take the empirical Bayesian approach described in Huertas et al. (2017) and Marquand, Brammer, et al. (2014a) finding the α and β that maximize the marginal likelihood of the observed data under our assumed model structure. With the prior as in Equations (3)–(5) and the likelihood as in Equation (6) the log marginal likelihood becomes:

$$\begin{aligned} \log p(\mathbf{y}|\alpha, \beta) = & -\frac{m}{2} \log(2\pi) + \frac{m}{2} \log(\beta) - \frac{1}{2} \log |\Sigma(\alpha)_{\text{prior}}| - \frac{1}{2} \log |\mathbf{A}| \\ & - \frac{1}{2} \mathbf{m}^T \Sigma(\alpha)_{\text{prior}}^{-1} \mathbf{m} - \frac{\beta}{2} (\mathbf{y} - \mathbf{X}\mathbf{m})^T (\mathbf{y} - \mathbf{X}\mathbf{m}) \end{aligned}$$

where $\mathbf{A} = \Sigma(\alpha)_{\text{prior}}^{-1} + \beta \mathbf{X}^T \mathbf{X}$ and $\mathbf{m} = \beta \mathbf{A}^{-1} \mathbf{X}^T \mathbf{y}$. We used *minimize*, a conjugate gradients optimizer available within the *gpml* toolbox (Rasmussen & Nickisch, 2010), which uses partial derivatives of the marginal likelihood with respect to each of the hyperparameters. We optimized these variables in the log domain to ensure positivity (see Appendix for further details).

In this article we predict the biomarker value at each subject's mean baseline and final follow-up ages, taking the probabilistic approach of integrating over all possible posterior model parameters. With the Gaussian posterior as in Equations (7)–(9) and the Gaussian likelihood $p(\mathbf{y}_*|\mathbf{X}_*, \mathbf{w}) = N(\mathbf{y}_*|\mathbf{X}_* \mathbf{w}, \beta^{-1}\mathbf{I}_m)$ of observing predictions \mathbf{y}_* given input \mathbf{X}_* , the predictive distribution that results from integration has a closed form solution (Rasmussen, 2006):

$$p(\mathbf{y}_*|\mathbf{X}_*, \mathbf{X}) = N\left(\mathbf{X}_* \bar{\mathbf{w}}, \beta^{-1} \mathbf{I} + \mathbf{X}_* \mathbf{A}^{-1} \mathbf{X}_*^T\right) \quad (10)$$

where $\mathbf{A} = \Sigma(\alpha)_{\text{prior}}^{-1} + \beta \mathbf{X}^T \mathbf{X}$ and \mathbf{X}_* is an $n \times nd$ design matrix with a row encoding either the mean baseline age or final sample age in this

case (or $2n \times nd$ to predict both at once). In general, we can predict an arbitrary number of time-points per subject by modifying \mathbf{X}_* accordingly.

For all models, we standardize (i.e., z-score) the training data across all subjects (the longitudinal observations \mathbf{y} and each nonconstant column of the design matrix \mathbf{X}) as well as the out-of-sample testing data (\mathbf{X}_* , using the means and standard deviations from \mathbf{X}) during model building and prediction. This ensures that all trajectories are modeled on a similar scale, which aids numerical stability when optimizing the hyperparameters. We rescale both the predictions and the estimated parameters back to their original dimensions for subsequent analysis (e.g., estimating annualized rates of change and group differences in parameters). With higher order models, the columns of \mathbf{X} may be highly correlated, leading to unstable variance estimates. In such cases, one may orthogonalize the columns prior to fitting the model.

We use the log Bayes factor, a ratio of the logarithm of model evidences (i.e., marginal likelihoods) to compare biomarker-information based coupling to random-information based coupling. Log Bayes factors are a principled way of comparing Bayesian models, under the assumption that each model has the same prior probability (Penny, 2012; Penny, Stephan, Mechelli, & Friston, 2004).

2.2 | Software: Model and figures

A MATLAB implementation of our method is available at <https://github.com/LeonAksman/bayes-mtl-traj>. The brain images in Figures 4–6, S8, S9, and S11 were produced via a command-line image render and snapshot tool, available at <https://github.com/LeonAksman/vtkSnap>.

2.3 | Simulations: Data generation

We created a simulation of subjects' trajectories that allowed us to compare several versions of our proposed model along with a baseline model. We simulated two scenarios: (a) linear trajectories with intercept variation: group differences in intercept with fixed slope and (ii) linear trajectories with slope variation: group differences in slope with fixed intercept. In both cases, we simulated 200 subjects' trajectories at each simulation run. To simulate intercept variation, for a given subject i we randomly selected an intercept w_{i0} from the set $\{-10, -8, -6, -4, -2\}$ and a fixed slope of $w_{i1} = -1$, and then randomly selected an initial measurement time t_{i1} between 0 and 10. We then generated three simulated samples with fixed time intervals: $y(t_{i1}) = w_{i0} + w_{i1}t_{i1} + \epsilon_{i1} = w_{i0} - t_{i1} + \epsilon_{i1}$, $y(t_{i2} = t_{i1} + 0.05) = w_{i0} - t_{i1} - 0.05 + \epsilon_{i2}$ and $y(t_{i3} = t_{i1} + 0.10) = w_{i0} - t_{i1} - 0.10 + \epsilon_{i3}$, where $\epsilon_{i1}, \epsilon_{i2}, \epsilon_{i3}$ are three independent measurement errors, each drawn from $N(0, \sigma_m)$. We simulated four different levels of measurement noise, $\sigma_m = 1, 2, 4, 8$. For each noise level, we made 30 simulation runs and evaluated nine different models (described below) on each run. We used the first two samples of each subject (t_{i1}, t_{i2} for subject i) to train each model and the third sample (t_{i3} for subject i) to evaluate out-of-sample prediction accuracy. The top row of Figure 1 provides an example of one simulation run for 200 subjects at each noise level.

TABLE 1 Models fit at each simulation run

Model	Purpose	Kernel	Covariance prior	# Cov. Hyper's
<i>random</i>	Allow both slope and intercept coupling via random biomarker	$K(r)_{SE}$	$\alpha_1 I_{2n} + \sum_{i=1}^2 (\alpha_{i1} I_n + \alpha_{i2} \mathbf{1}_n + \alpha_{i3} K(r)_{SE}) \otimes M_{ii}$	9
<i>linear both</i>	Allow both slope and intercept coupling via true biomarker	$K(b)_{linear}$	$\alpha_1 I_{2n} + \sum_{i=1}^2 (\alpha_{i1} I_n + \alpha_{i2} \mathbf{1}_n + \alpha_{i3} K(b)_{linear}) \otimes M_{ii}$	7
<i>Gaussian both</i>	Allow both slope and intercept coupling via true biomarker	$K(b)_{SE}$	$\alpha_1 I_{2n} + \sum_{i=1}^2 (\alpha_{i1} I_n + \alpha_{i2} \mathbf{1}_n + \alpha_{i3} K(b)_{SE}) \otimes M_{ii}$	9
<i>linear int</i>	Allow intercept coupling via true biomarker	$K(b)_{linear}$	$\alpha_1 I_{2n} + (\alpha_{11} I_n + \alpha_{12} \mathbf{1}_n + \alpha_{13} K(b)_{linear}) \otimes M_{11}$ $+ (\alpha_{21} I_n + \alpha_{22} \mathbf{1}_n) \otimes M_{22}$	6
<i>Gaussian int</i>	Allow intercept coupling via true biomarker	$K(b)_{SE}$	$\alpha_1 I_{2n} + (\alpha_{11} I_n + \alpha_{12} \mathbf{1}_n + \alpha_{13} K(b)_{SE}) \otimes M_{11}$ $+ (\alpha_{21} I_n + \alpha_{22} \mathbf{1}_n) \otimes M_{22}$	7
<i>linear slope</i>	Allow slope coupling via true biomarker	$K(b)_{linear}$	$\alpha_1 I_{2n} + (\alpha_{11} I_n + \alpha_{12} \mathbf{1}_n) \otimes M_{11}$ $+ (\alpha_{21} I_n + \alpha_{22} \mathbf{1}_n + \alpha_{23} K(b)_{linear}) \otimes M_{22}$	6
<i>Gaussian slope</i>	Allow slope coupling via true biomarker	$K(b)_{SE}$	$\alpha_1 I_{2n} + (\alpha_{11} I_n + \alpha_{12} \mathbf{1}_n) \otimes M_{11}$ $+ (\alpha_{21} I_n + \alpha_{22} \mathbf{1}_n + \alpha_{23} K(b)_{SE}) \otimes M_{22}$	7
<i>plain</i>	No biomarker based coupling	None	$\alpha_1 I_{2n} + (\alpha_{11} I_n + \alpha_{12} \mathbf{1}_n) \otimes M_{11}$ $+ (\alpha_{21} I_n + \alpha_{22} \mathbf{1}_n) \otimes M_{22}$	5
OLS	No coupling	None	$\alpha_1 I_{2n}, \alpha_1 \rightarrow \infty$	0

Note. Last column contains number of hyperparameters in given covariance prior.

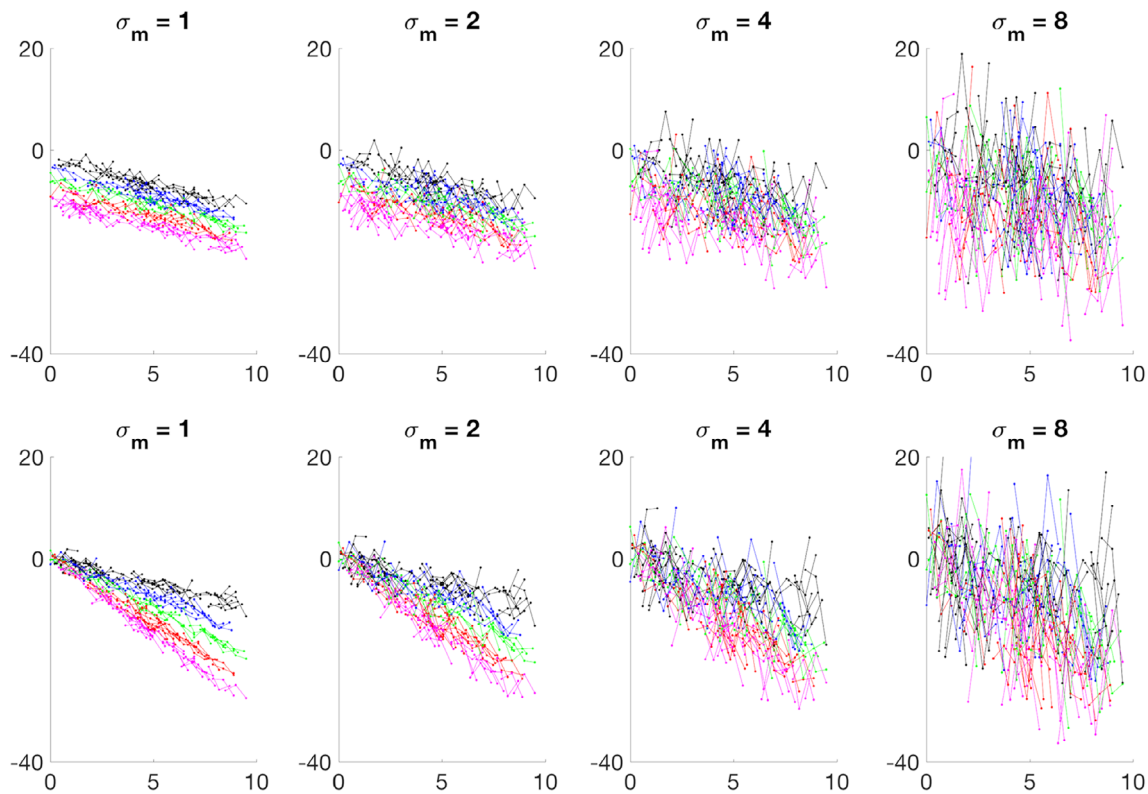


FIGURE 1 Top row: One run of the simulation of 200 subjects' longitudinal samples with group differences in intercept at four different measurement noise (σ_m) levels. Bottom row: The same with group differences in slope. Each subject has three samples, with trajectory parameters chosen from among five gradations of intercept (top row) or slope (bottom row), indicated by different colors [Color figure can be viewed at wileyonlinelibrary.com]

To simulate slope variation, for a given subject i we randomly selected a slope w_{i1} from the set $\{-1.0, -1.5, -2.0, -2.5, -3.0\}$ and a fixed intercept of $w_{i1} = 0$. We randomly selected t_{i1} as before and

generated $y(t_{i1})$, $y(t_{i2} = t_{i1} + 0.05)$, and $y(t_{i3} = t_{i1} + 0.10)$ with measurement errors $\epsilon_{i1}, \epsilon_{i2}, \epsilon_{i3}$ drawn from $N(0, \sigma_m)$. We used the same four measurement noise levels and again made 30 simulation runs,

generating 200 simulated subjects' trajectories for each noise level. We evaluated the same nine models using the first two samples of each subject for training and the third for prediction. The bottom row of Figure 1 provides an example of one simulation run at each noise level.

2.4 | Simulations: Model building

We investigated how different variations of the model, with and without biomarker-kernel-based coupling (i.e., via the \mathbf{K}_j matrices described above), performed under the two parameter variation scenarios and the four measurement noise levels. We created a 200×1 biomarker vector \mathbf{b} as a noisy measure of the group difference in the parameters, so that the i^{th} element of \mathbf{b} was $b_i = w_{i0} + \varepsilon_i$ under intercept variation and $b_i = w_{i1} + \varepsilon_i$ under slope variation, with ε_i drawn from $N(0, 1)$ in both cases.³ Using this biomarker, we compared two commonly used similarity matrices: (a) a rank-one approximation $\mathbf{K}(\mathbf{b})_{\text{linear}} = \mathbf{b}\mathbf{b}^T$ (the outer product of \mathbf{b} with itself); and (b) a squared exponential (SE) kernel (also referred to as a Gaussian radial basis function kernel) $\mathbf{K}(\mathbf{b})_{\text{SE}}$, with $k_{ij} = \exp(-\sigma_{\text{SE}}\|b_i - b_j\|^2)$ in the i^{th} row and j^{th} column, where we make the dependence of these matrices on the input explicit. The term $\sigma_{\text{SE}} > 0$ is a parameter that gives the kernel additional scaling flexibility. It is also possible to encode categorical (i.e., group) membership via a binary similarity matrices rather than an SE kernel, with one indicating two subjects belong to the same class and zero otherwise.

When using SE kernels, we treated the σ_{SE} term as a covariance prior hyperparameter (in addition to the α 's in Equations [4] and [5]). We formed six different models using these two kernels: "linear both" and "Gaussian both" had covariance prior structure as in Equations (4) and (5), parameterizing full independence, full coupling and kernel-based coupling in both the intercept and slope parameters. The "linear int" and "Gaussian int" models restricted kernel-based coupling to the intercepts: referring to Equations (4) and (5) and assuming one coupling kernel \mathbf{K}_1 , this means we allow a \mathbf{K}_1 term in Σ_{c2} but not in Σ_{c1} . The "linear slope" and "Gaussian slope," in contrast, restricted kernel-based coupling to the slopes, allowing a \mathbf{K}_1 term in Σ_{c2} but not in Σ_{c1} . These latter four models allowed us to test the effect of "oracle-like" (i.e., with perfect *a priori*) knowledge of simulation scenario: e.g., whether the two "int" models outperform other models in the variable intercept, fixed slope scenario. In such cases, biomarker-based coupling of slopes in the intercepts variation case (or vice versa) is extraneous and may lead to spurious inference of group differences if a model is allowed to infer coupling where none exists.

We compared biomarker coupled models to several simpler coupled models. The simplest of these was the "OLS" model, an uncoupled model which asymptotically corresponds to a Bayesian model with a parameter covariance prior of $\alpha_1 \mathbf{I}_{2n}$ with α_1 tending to infinity (i.e., a high prior uncertainty on all parameters for all subjects). The second model, "plain," trades off fully independent and fully coupled covariance priors, without any kernel-based coupling. It is

very similar to an LME model with random intercepts and random slopes. To understand the role of kernel-based coupling, we compared biomarker-kernel coupled models to random-information-kernel coupled models. We formed a 200×1 vector \mathbf{r} with each element drawn from $N(0, 1)$, so that each subject was assigned a random number, and formed another SE kernel $\mathbf{K}(\mathbf{r})_{\text{SE}}$ based on it. We used this to create "random," parametrized exactly as "Gaussian both." See Table 1 for further model details.

We compared our approach to standard LME modeling using the LME implementation available in *Freesurfer* (Bernal-Rusiel et al., 2013; Bernal-Rusiel, Reuter, Greve, Fischl, & Sabuncu, 2013).⁴ Specifically, we built two LME models, with fixed effects of baseline age and baseline biomarker value and either random intercepts (termed "LME: *rl*") or random intercepts and slopes ("LME: *rl, rs*").

We also compared our empirical Bayesian approach, which produces point estimates of hyperparameter priors (i.e., an estimate of prior means with zero variance) to a fully Bayesian approach, in which we place priors on the hyperparameters and estimate their posterior distribution. In this way, the fully Bayesian approach accounts for the hyperparameter uncertainty, which may improve parameter and prediction coverage by improving the estimation of their uncertainties. We compared the empirical Bayesian version of "plain," with five covariance hyperparameters (the α 's) and one inverse observation noise parameter (β) to a fully Bayesian model with the same covariance structure. We placed broad, uninformative half-normal priors on the α 's, by setting each $\alpha \sim \text{normal}(0, 100)$ with constraint $\alpha > 0$, and an inverse Gamma distribution on β^{-1} , setting $\beta^{-1} \sim \text{InvGamma}(1, 1)$. We used Markov chain Monte Carlo (MCMC) to estimate the full model as it was no longer analytically tractable to derive all the necessary posterior distributions. We implemented the full model in *Stan* (Carpenter et al., 2017) using Hamiltonian Monte Carlo. Due to the significantly longer running times of the full model, (see Results) we ran the same two simulation scenarios for 50 instead of 200 subjects, with all other settings as before. We used the default parameters for MCMC sampling: four chains, with 1,000 warm-up iterations and 1,000 sampling iterations per chain, so that the posterior distributions had 4,000 sampling iterations in total. We checked the convergence of the chains' posterior distributions using the R metric provided. We checked the quality of the chain by looking at the means, Markov chain standard errors (MCSE) and effective sample sizes of the hyperparameters.

Finally, we performed additional simulations to test our assumption of independent measurement noise, parameterized by β in Equation (6), choosing five representative models in all cases: "Gaussian both" and "plain" MTL models plus the two LME models and "OLS." In the first set of simulations, we varied the amount of within-subject noise correlation by instead allowing a block diagonal noise structure. For each subject's measurements, we used a noise covariance with $\sigma_m^2 = 4$ on the diagonal and all off-diagonal terms set to $\rho\sigma_m^2$, so that we recover uncorrelated noise when $\rho = 0$ and perfectly correlated noise (i.e., the same for all observations over time) when $\rho = 1$. We simulated with three levels of ρ (0, 0.5, 0.75). In the second set of simulations used three levels of

³We do not vary the biomarker noise here as we found that, in general, it did not have a strong effect on the models, particularly as compared to the measurement noise.

⁴<https://surfer.nmr.mgh.harvard.edu/fswiki/LinearMixedEffectsModels>.

noise skewness: zero (Gaussian, as before), 0.6 (slightly skewed), and 0.9 (highly skewed), with $\sigma_m^2 = 4$ in all cases.

2.5 | Simulations: Model evaluation

Parametric Bayesian modeling provides probabilistic predictions (via Equation [10]) and parameter distributions (via Equations (7)–(9)). We can thus compare the performance of models in terms of both their accuracy of predicting ground truth trajectories and how well they estimate model parameters. The latter objective is potentially important when there are group differences in trajectories, for example, when a disease group has a steeper rate of gray matter volume decline in a ROI compared to a healthy control group. In such a case, using linear models we should be able to detect a difference in the slope parameters across the groups and, assuming the decline starts from the same level, no corresponding difference in intercepts.

For each model, we evaluated the mean absolute error (MAE) of predicting subjects' held-out samples and quantified the accuracy of the inferred trajectory parameters (intercepts and slopes) via coverage probability and MAE measures. We defined the coverage probability as the fraction of times the true value of a parameter (intercept or slope) falls within two standard deviations of its estimated value, that is, within the posterior credible interval of the parameter. As this is a 95% credible interval a coverage probability of 0.95 is an ideal outcome. For the Bayesian MTL models, we can easily calculate these quantities using the posterior means and variances (Equations (7)–(9)). For the LME models, direct estimates of the posterior parameter variance were not available: we therefore estimated them by adding the fixed effect and random effect variance estimates of the intercept and slope when appropriate.

In practice, the coverage probability may not be sufficient for understanding how accurately a model estimates a parameter as a model may simply estimate a high enough variance so that the true value is always covered. For this reason, we also computed the error (MAE) between the estimated parameters (intercept, slope) and their known true values.

2.6 | ADNI application: Dataset

Data used in the preparation of this article were obtained from the Alzheimer's disease neuroimaging initiative (ADNI) database (adni.loni.usc.edu). The ADNI was launched in 2003 as a public–private partnership, led by Principal Investigator Michael W. Weiner, MD. The primary goal of ADNI has been to test whether serial magnetic resonance imaging (MRI), positron emission tomography (PET), other biological markers, and clinical and neuropsychological assessment can be combined to measure the progression of mild cognitive impairment (MCI) and early Alzheimer's disease (AD). For up-to-date information, see www.adni-info.org.

We used ADNI subjects with at least one [18 F]-Florbetapir PET scan, which images brain amyloid accumulation, using the earliest available

image as the baseline time-point. We chose a subset of 437 subjects: 104 cognitively normal (CN), 243 MCI, 90 probable Alzheimer's disease (AD). Each had at least three MRIs at or after the chosen baseline, with a total of 1,545 images across all subjects. There were 257 subjects with three MRIs, 138 subjects with four MRIs, 31 subjects with five MRIs, 10 subjects with six MRIs and one subject with seven MRIs.

We processed the PET scans to derive standardized uptake value ratio (SUVR) values in cortical gray matter as measures of cortical amyloid deposition at baseline, defined here as the first Florbetapir scan available. Details of PET image processing can be found in Scelsi et al. (2018). Briefly, tracer uptakes in the cortical ROI were standardized to the uptake in a composite reference region following recommendations from (Landau et al., 2015). We also used amyloid- β , total tau and phosphorylated tau (pTau) from CSF measured at or before baseline as measures of severity of amyloid and tau pathology. Lastly, we retrieved subjects' apolipoprotein E (APOE) genetic information, particularly the number of $\epsilon 2$ and $\epsilon 4$ alleles (Harold et al., 2009; Liu, Kanekiyo, Xu, & Bu, 2013).

We parcellated the T1-weighted images using geodesic information flows (GIF; Cardoso et al., 2015), creating 20 cortical sub-lobe volumes from each image (see Figure S7 for the list of ROIs). We then normalized each of these ROIs using each subject's total intracranial volume (TIV). Normalized ROIs were subsequently used for longitudinal trajectory modeling and out-of-sample prediction. We withheld the final follow-up ROI from each model to test the out-of-sample prediction accuracy of our models.

2.7 | ADNI application: Model building

We built eight different types of models, detailed in Table 2, for each of the 20 regions for a total of 160 models.

We used first order (linear) polynomial models for all regions: previous work has shown this is a reasonable assumption for modeling cortical trajectories (Ziegler et al., 2015). Based on our simulations (see Results), we chose the “Gaussian both” type of model when using biomarker coupling, allowing both intercept and slope coupling, assuming no prior knowledge of the type of coupling that exists in the data. We formed four different kernels (\mathbf{K}_1 , \mathbf{K}_2 , \mathbf{K}_3 , \mathbf{K}_4) based on true biomarkers along with a fifth kernel based on a random biomarker-based kernel ($\mathbf{K}_5 = \mathbf{K}(\mathbf{r})_{SE}$, \mathbf{r} a vector of random values) as in the simulations. Kernels $\mathbf{K}_i = \mathbf{K}(\mathbf{b}_i)_{SE}$, $i = 1, 2, 3$ were formed using: (a) \mathbf{b}_1 , a vector of SUVR values across subjects derived from amyloid PET, (b) $\mathbf{b}_2 = \log(\mathbf{tau}/\mathbf{A}\beta)$, a vector encoding the relationship between CSF tau, which increases in subjects with AD, and CSF amyloid- β , which decreases in those with AD (Sunderland et al., 2003), log transformed to improve normality, and (c) \mathbf{b}_3 , a vector encoding CSF pTau (Hampel et al., 2010).

To encode the APOE genetic similarity between subjects we used the weighted identity by state (weighted-IBS) kernel function as in Kwee et al., (Kwee, Liu, Lin, Ghosh, & Epstein, 2008):

$$k_{IBS,ij} = \frac{w_{\epsilon 2} IBS_{ij, \epsilon 2} + w_{\epsilon 4} IBS_{ij, \epsilon 4}}{w_{\epsilon 2} + w_{\epsilon 4}} \quad (12)$$

TABLE 2 Models fit for ADNI data

Model	Purpose	Kernel(s)	Covariance prior	# Cov. Hyper's
<i>multiple</i>	Allow coupling via all four true biomarkers	$\mathbf{K}_1, \mathbf{K}_2, \mathbf{K}_3, \mathbf{K}_4$	$\alpha_1 \mathbf{I}_{2n} + \sum_{i=1}^2 (\alpha_{i1} \mathbf{I}_n + \alpha_{i2} \mathbf{1}_n + \sum_{j=1}^4 \alpha_{i(2+j)} \mathbf{K}_j) \otimes \mathbf{M}_{ii}$	21
<i>PET amyloid</i>	Allow coupling via SUVR similarity	$\mathbf{K}_1 = \mathbf{K}(\mathbf{b}_1)_{SE}$	$\alpha_1 \mathbf{I}_{2n} + \sum_{i=1}^2 (\alpha_{i1} \mathbf{I}_n + \alpha_{i2} \mathbf{1}_n + \alpha_{i3} \mathbf{K}_1) \otimes \mathbf{M}_{ii}$	9
<i>CSF tau/aBeta</i>	Allow coupling via tau/aBeta similarity	$\mathbf{K}_2 = \mathbf{K}(\mathbf{b}_2)_{SE}$	$\alpha_1 \mathbf{I}_{2n} + \sum_{i=1}^2 (\alpha_{i1} \mathbf{I}_n + \alpha_{i2} \mathbf{1}_n + \alpha_{i3} \mathbf{K}_2) \otimes \mathbf{M}_{ii}$	9
<i>CSF pTau</i>	Allow coupling via pTau similarity	$\mathbf{K}_3 = \mathbf{K}(\mathbf{b}_3)_{SE}$	$\alpha_1 \mathbf{I}_{2n} + \sum_{i=1}^2 (\alpha_{i1} \mathbf{I}_n + \alpha_{i2} \mathbf{1}_n + \alpha_{i3} \mathbf{K}_3) \otimes \mathbf{M}_{ii}$	9
<i>APOE</i>	Allow coupling via APOE ϵ_2 , ϵ_4 allele similarity	$\mathbf{K}_4 = \mathbf{K}_{\text{expIBS}}$	$\alpha_1 \mathbf{I}_{2n} + \sum_{i=1}^2 (\alpha_{i1} \mathbf{I}_n + \alpha_{i2} \mathbf{1}_n + \alpha_{i3} \mathbf{K}_4) \otimes \mathbf{M}_{ii}$	9
<i>random</i>	Allow coupling via random biomarker	$\mathbf{K}_5 = \mathbf{K}(r)_{SE}$	$\alpha_1 \mathbf{I}_{2n} + \sum_{i=1}^2 (\alpha_{i1} \mathbf{I}_n + \alpha_{i2} \mathbf{1}_n + \alpha_{i3} \mathbf{K}_5) \otimes \mathbf{M}_{ii}$	9
<i>plain</i>	No biomarker based coupling	None	$\alpha_1 \mathbf{I}_{2n} + (\alpha_{11} \mathbf{I}_n + \alpha_{12} \mathbf{1}_n) \otimes \mathbf{M}_{11} + (\alpha_{21} \mathbf{I}_n + \alpha_{22} \mathbf{1}_n) \otimes \mathbf{M}_{22}$	5
<i>OLS</i>	No coupling	None	$\alpha_1 \mathbf{I}_{2n}, \alpha_1 \rightarrow \infty$	0

Note. Last column contains number of hyperparameters in given covariance prior.

where the $\text{IBS}_{ij, \epsilon_2}$, $\text{IBS}_{ij, \epsilon_4}$ terms (each taking values 0, 1, or 2) refer to the number of ϵ_2 and ϵ_4 alleles shared by subjects i and j . The inverse minor allele frequency ($1/\text{MAF}$) weights w_{ϵ_2} , w_{ϵ_4} serve to up-weight rarer SNPs. The range of this function is between zero and two. To better compare to the other SE kernels, we created an exponentiated version of this kernel function:

$$k_{\text{expIBS}, ij} = \exp(-\sigma(2 - k_{\text{IBS}, ij})) \quad (13)$$

that includes a scaling hyperparameter σ and has a range between zero and one. We formed the \mathbf{K}_4 kernel matrix using this kernel function.

We also compared our approach to (Freesurfer-based) LME models. We built three LME models with fixed effects of age and baseline amyloid load (measured via PET SUVR, as in the “*PET amyloid*” MTL model) and either random intercepts (termed “*Rand Int*”), random intercepts and slopes (“*Rand Int/Slp*”) or random intercepts, random slopes, and random amyloid (“*Rand Int/Slp/Amyloid*”).

3 | RESULTS

3.1 | Simulations: Results

Figure 2 depicts boxplots of the prediction MAEs across simulation runs. Models using SE kernel-based coupling (“*Gaussian*” type models) generally performed better than their linear kernel counterparts (“*linear*” type models). The advantage of the SE kernel in some cases may be attributable to the ability to tune the kernel width (the σ_{SE} term) as an additional hyperparameter, which adds scale flexibility. “*Gaussian both*” was consistently among those with lowest MAE. We expected the oracle-like models (“*int*” type in top row, “*slope*” type in bottom, marked with asterisks in the figures) to outperform the other models, however, overall, they perform similarly to the other models in most cases. Importantly, all

MTL based models (including “*plain*”) outperform “*OLS*” by a large margin, roughly halving the error. Figure S1 depicts histograms of parameter estimates for both “*plain*” and “*OLS*” for a representative simulation run, showing that the Bayesian model shrinks both the slopes and intercepts to their respective group mean, decreasing the variance of the estimates considerably. The shrinkage also results in a small increase in bias, evidenced by the larger distance between the parameter means of “*plain*” (dashed red line) to the true parameter means (dashed black line) compared to “*OLS*” (dashed blue line), with an overall large decrease in the mean squared errors of the parameter estimates (“*plain*”: 8.8 for intercepts, 0.4 for slopes; “*OLS*” 193.0 for intercepts, 8.1 for slopes).

The two LME models also performed well, with similar MAEs to the “*Gaussian*” models. Figure S2 depicts the corresponding prediction coverage probabilities, showing that both the MTL and LME models’ predictions cover the true target value at close to the ideal rate of 0.95, again outperforming “*OLS*” by a large margin, especially at higher noise levels. We also observe that the simpler MTL models (“*linear*” models, along with “*plain*”) have both high coverage in Figure S2 and relatively high MAE in Figure 2, meaning that, compared to the other MTL and LME models, they make relatively inaccurate predictions but estimate high enough measurement uncertainty to cover the true target value.

Figure 3 depicts the corresponding parameter coverage probabilities and estimation errors. In the fixed slope, varying intercepts scenario (top row), coverage of the true fixed slope parameter was high for all models (at or near 100%, exceeding the nominal level of 95%) while intercept coverage varied greatly across models and noise levels. The LME models generally did not cover the true intercept values as frequently as the MTL models, particularly the random intercepts (“*LME: rI*”). The random intercepts, random slopes model (“*LME: rI, rS*”) performed better at higher noise levels, but was generally outperformed by the MTL models. One possible explanation is that the MTL models explicitly model parameter uncertainty as part of their Bayesian formulation, while we have had to estimate the LME models’ overall parameter uncertainty by combining the associated

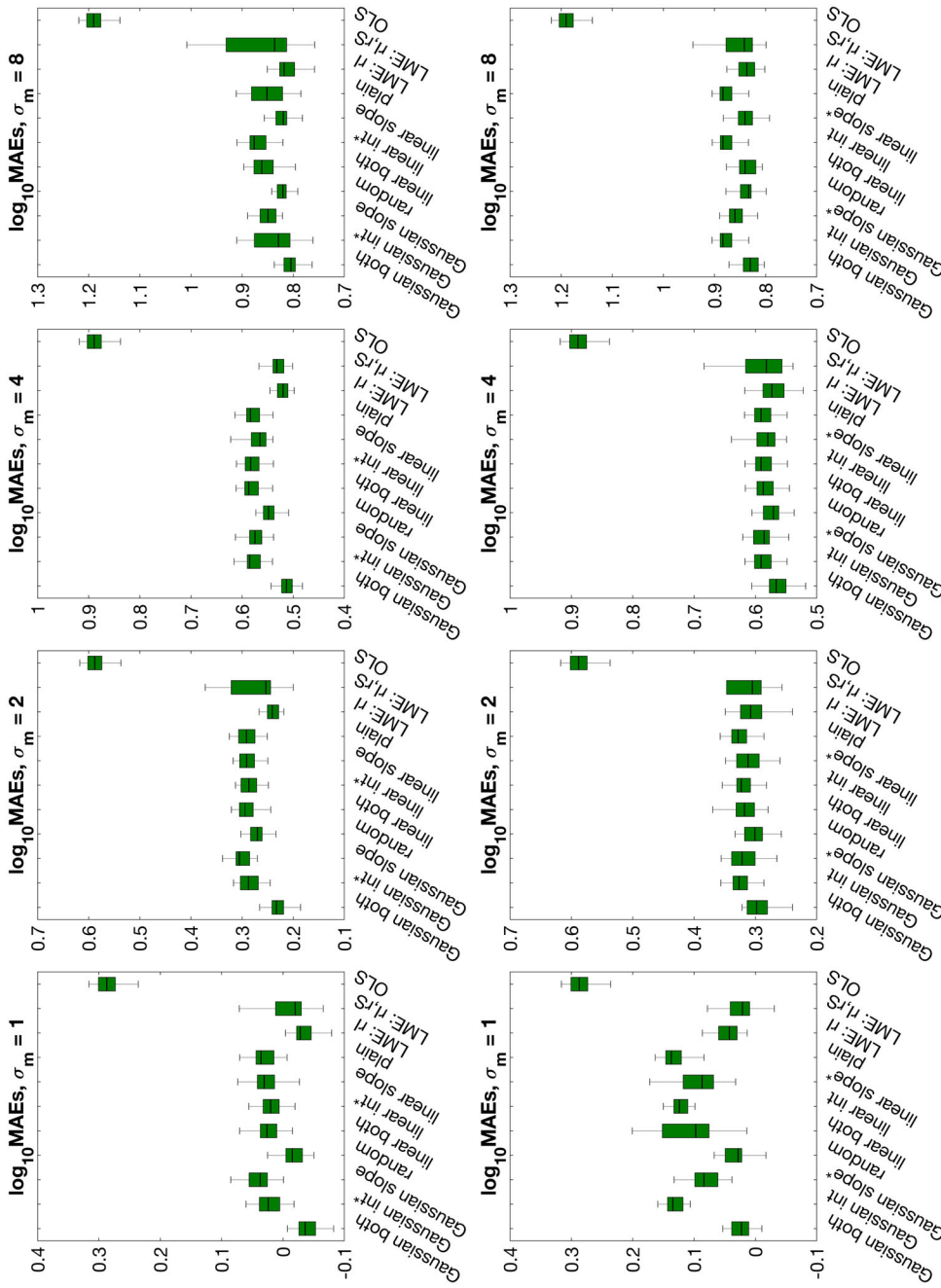


FIGURE 2 Boxplots of log mean absolute errors (MAEs) of predictions of all models across all simulations runs for the two scenarios: intercept variation (top row) and slope variation (bottom row) for four levels of measurement noise (σ_m). Models with oracle-like prior information are marked with an asterisk (top row: "int" models; bottom row: "slope" models) [Color figure can be viewed at wileyonlinelibrary.com]

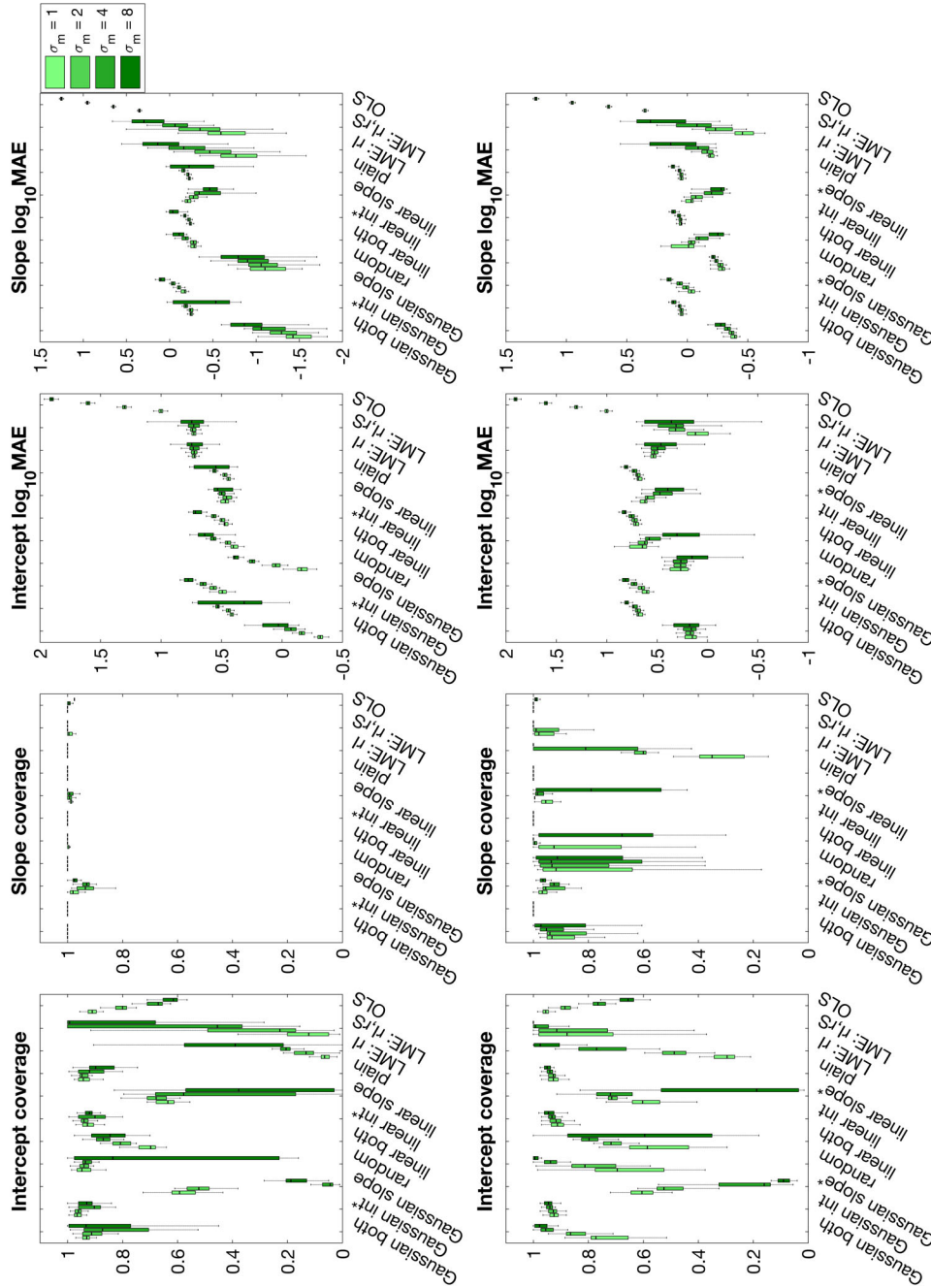


FIGURE 3 Boxplots of parameter coverage probabilities (i.e., fractions of times the true parameter value fell within the posterior credible region) and log mean absolute errors (MAE) between estimated and actual parameters for the two scenarios: intercept variation (top row) and slope variation (bottom row) for four measurement noise levels (σ_m). Models with oracle-like prior information are marked with an asterisk (top row: "slope" models; bottom row: "int" models) [Color figure can be viewed at wileyonlinelibrary.com]

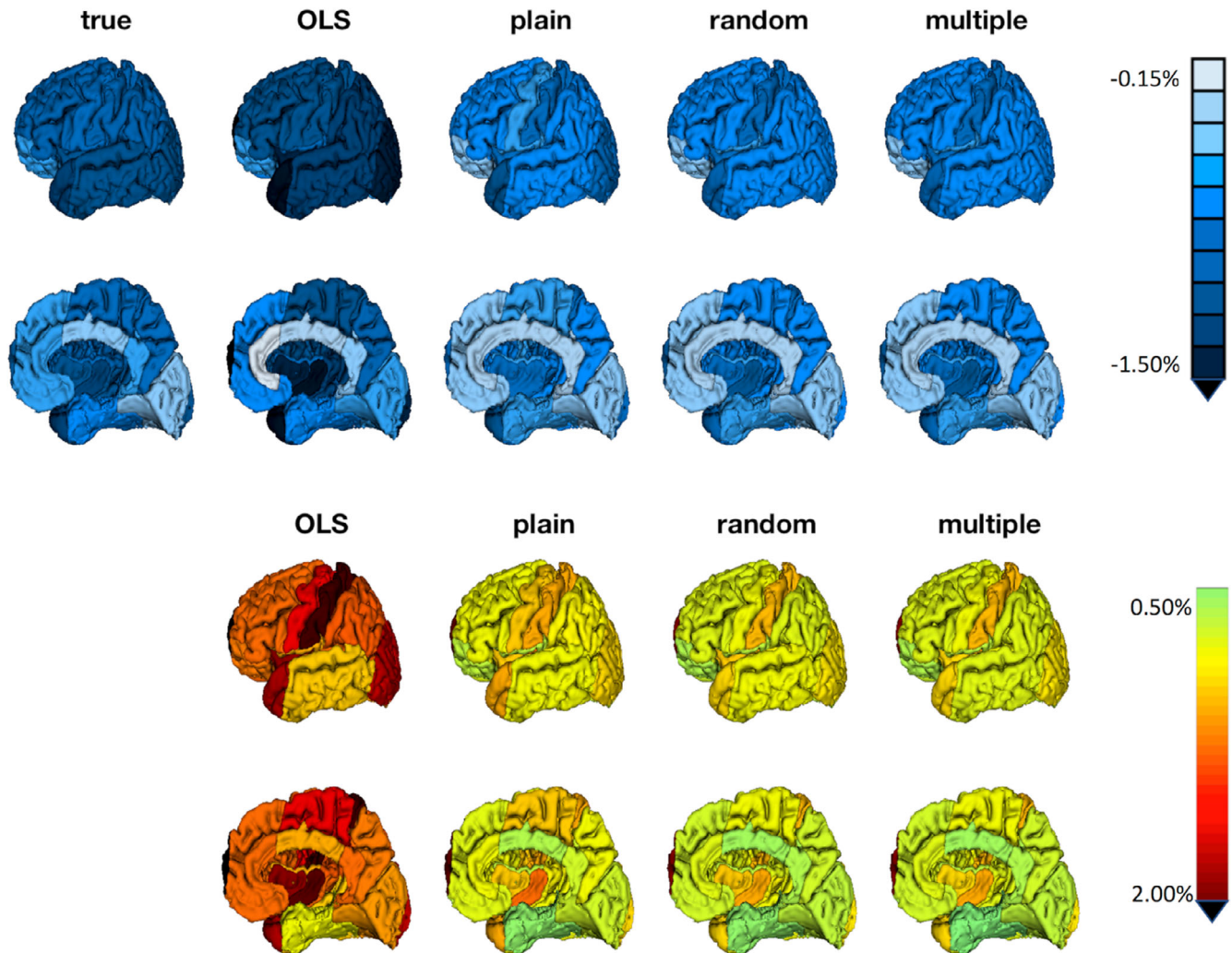


FIGURE 4 Top: True and estimated annualized rates of change across cortex for four representative MTL models bottom: MAEs of estimates. MAE, mean absolute error [Color figure can be viewed at wileyonlinelibrary.com]

fixed and random effect uncertainties. In addition, the LME models also have higher parameter estimation errors (the intercept and slope log MAE figures in the top row), which measures the quality of parameter mean estimates rather than variances. Overall in this scenario the “Gaussian” models outperformed all others in terms of parameter coverage and estimation error while the “linear” models and “plain” were comparable to the LME models in terms of parameter estimation error.

In the second scenario, fixed intercept and varying slopes (Figure 3, bottom row), the “Gaussian” models performed well in both parameter coverage and parameter estimation error; in this case, the two LME models also performed competitively. “LME: rI , rS ” had consistently highest intercept and slope coverage and lowest parameter estimation errors at low measurement noise levels, reflecting the fact that the random slopes assumption is appropriate in this scenario. However, this model's parameter estimation error, particularly the slope MAE, increases sharply with higher measurement noise levels while the “Gaussian” models are relatively unaffected.

The two simulation scenarios suggest that the “Gaussian” style MTL models are a good choice for both prediction and parameter inference and compare favorably with standard LME models in many cases. Among these, “Gaussian both” is appealing, as it makes no *a priori* assumptions on the type of coupling that exists within the data. Therefore, we used this type of model throughout our experiments with the Alzheimer's study data.

Figure S3, part A shows the empirical Bayesian implementation of “plain” (“EB plain”) has very similar predictive performance to the full Bayesian implementation (“MCMC plain”) in terms of prediction error. Both have high coverage of the true target values though the full Bayesian model is consistently closer to the optimal coverage of 0.95 while the empirical Bayesian model is prone to underestimating the predictive uncertainty. Figure S3, part B depicts the parameter estimation metrics: the full Bayesian model has much higher coverage of the intercept in both scenarios; both models have similarly high coverage of the slope. The full Bayesian model has lower error in estimating the true values of both intercepts and slopes in both scenarios. We briefly compared the computation times of the two

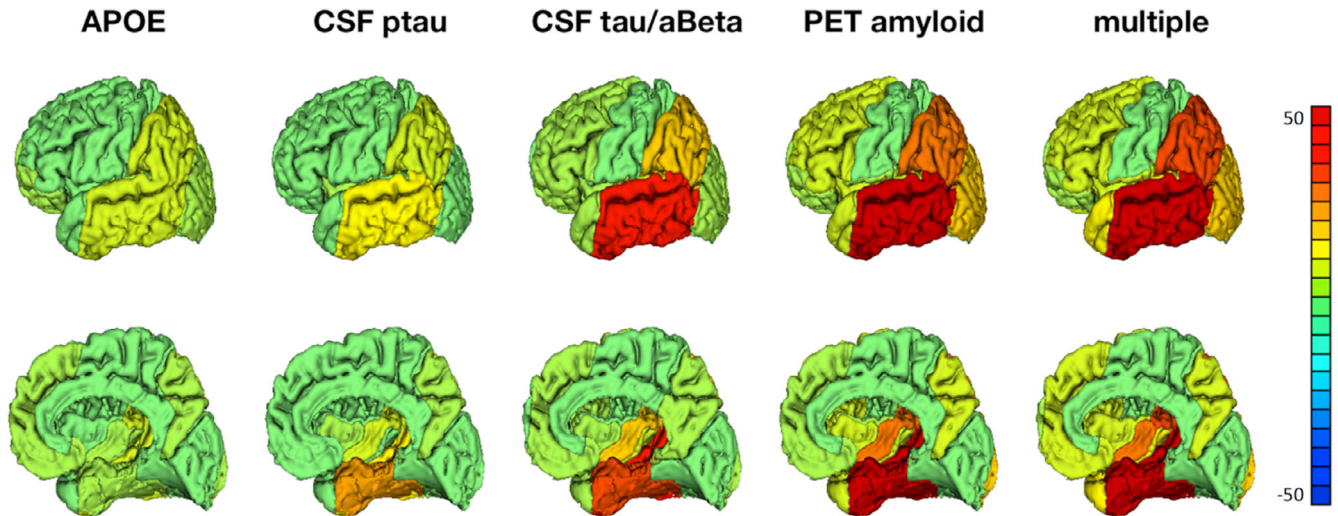


FIGURE 5 Log Bayes factors across cortex, comparing each biomarker-coupled MTL model to “random” [Color figure can be viewed at wileyonlinelibrary.com]

models on a single run of the intercept varying scenario with 20, 50, and 100 subjects: the empirical Bayesian model took 0.13, 0.38, and 0.50 seconds, respectively, while the full Bayesian model was considerably slower: 51,398 and 4,356 seconds, respectively. Table S1 gives the convergence diagnostics for the posterior estimates of the hyperparameters of “MCMC plain” for one run of the intercept varying scenario. The estimates appear to have converged: all R values were at their ideal values of one, the number of effective samples (N_{eff}) was high in all cases and the MCSE's were small compared to the estimated posterior means, so that the 95% confidence intervals on the means did not cross zero.

Figure S4 depicts results from the simulations that varied noise correlation while Figure S5 depicts those with varied skewness. In Figure S4, part A, we observe that the prediction related metrics are similar between “Gaussian both” and the two LME models in both simulations scenarios and that all models' prediction errors fall as noise correlation increases. Figure S4, part B shows corresponding parameter estimation metrics for both scenarios: “Gaussian both” outperforms the LME models on intercept coverage and parameter error in the intercept varying scenario (top row) but “LME: r_l , r_s ” has near optimal coverage in the slope varying scenario (bottom row), where the random slopes assumption is appropriate. However, these two models are similar in terms of slope coverage and both intercept and slope estimation errors. Figure S5, part A depicts the three different levels of measurement error skewness that we used in the second set of simulations. In this case, we observe that varying skewness does not substantially affect any of the models' prediction or parameter estimation metrics. Again, in general “Gaussian both” and the two LME models have similar prediction coverages and errors (part B), while “Gaussian both” outperforms the LME models in parameter estimation in the intercepts varying scenario (part C, top) and has similarly good performance in the slopes varying scenario (part C, bottom).

3.2 | ADNI application: Results

The likelihood term in Equation (6) assumes that observations are normally distributed about their mean (i.e., the residuals are normal) and uncorrelated over time within each subject. We tested the impact of these assumptions on ADNI modeling by comparing the histograms of residuals for two models in Figure S6: “CSF tau/aBeta,” which was representative of the biomarker-coupled MTL models, and “OLS,” the uncoupled reference model. Across all regions, the residuals of “CSF tau/aBeta” are much closer to being normally distributed than those of “OLS.” We also tested for heteroscedasticity, calculating the correlation of residuals to baseline age across subjects and found no significant correlation in both models for any region.

Figure 4 (top part) depicts the true and estimated annualized rates of change across the 20 cortical ROIs for four representative models (“OLS,” “plain,” “random,” “multiple”). Note that there is no information exchange between ROIs; in its presented form our method is univariate, coupling across subjects within each ROI and modeling ROIs separately. We computed the true annualized rate of change by dividing the percentage change from baseline to final (held-out) follow-up by the number of elapsed years. We note that this true annualized rate is essentially a two-point OLS estimate and is therefore more a silver than a gold standard. We see most of the cortex degenerating by 0.33% (middle cingulate) to 1.3% (posterior insula) annually, with the lateral regions generally degenerating faster than the medial regions. We computed the models' estimated annualized rates using their predictions of the held-out sample instead of the true held-out value. Figure 4 (bottom) depicts the associated MAEs of these predictions, with the three MTL models (“plain,” “random,” “multiple”) having lower MAEs than the “OLS” model across most ROIs. The two kernel coupled models (“random” and “multiple”) have further decreased MAEs compared to “plain,” though there is no further discernible difference in MAE between the two.

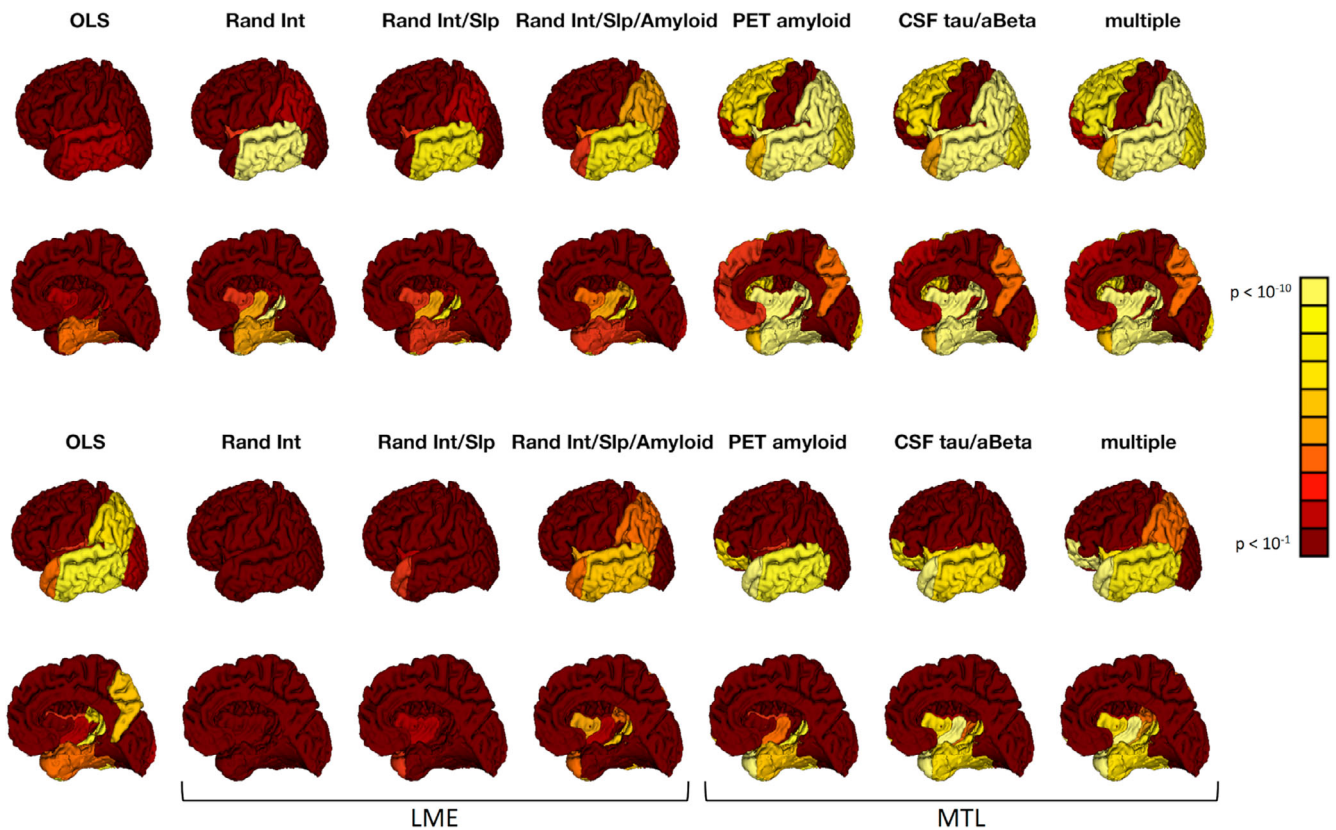


FIGURE 6 Top: Significance of (cross-sectional) diagnostic group differences in predicted volume at mean baseline age (73.5 years) for OLS, LME, and selected MTL models bottom: same for (longitudinal) group differences in estimated slopes [Color figure can be viewed at wileyonlinelibrary.com]

Figure S7 provides a quantitative comparison of prediction error across all OLS plus MTL models. We performed *t*-tests on the difference in absolute error between models to understand the effect of various modeling choices, showing: (a) all MTL model errors are significantly lower than those of “OLS” across all ROIs bar the lateral temporal region (where only “plain” and “random” have higher error than “OLS”); (b) there is further improvement due to kernel coupling, evidenced by significantly lower absolute errors in at least one model relative to “plain” in 13 out of 20 ROIs; (c) as in simulations, there is a small difference in error between random-information-based and biomarker-based kernel coupling, with some biomarker-based models having significantly lower error than “random” (within 10 ROIs: anterior insula, DLPFC, lateral occipital, lateral parietal, lateral temporal, medial parietal, medial temporal, posterior cingulate, supratemporal, and temporal pole regions). Statistical tests were Bonferroni corrected for 320 (eight models \times 20 ROIs \times 2 parameter types) comparisons. Furthermore, Figure S8 depicts the MAEs of predicting annualized rate of change for three LME models (described in Methods) built using the same information as in “PET amyloid.” All models had very similar MAEs across ROIs in this case.

Figure 5 depicts log Bayes factors across cortical regions for the comparison of the five biomarker-coupled MTL models to “random,” showing “CSF tau/aBeta,” “PET amyloid” and “multiple” have the largest and most widespread improvements in model evidence. We also see

that “multiple” is most similar to “PET amyloid,” the best individual biomarker coupled model in terms of model evidence, providing some assurance that combining kernels works as expected.

Figure 6 depicts the significance of diagnostic group differences (CN, MCI, or AD) in subjects’ estimated parameters across OLS, LME, and MTL assessed via one-way analysis of variance (ANOVAs) and Bonferroni corrected for 480 (12 model comparisons \times 20 ROIs \times 2 parameter types) comparisons. The three models with highest model evidence are depicted in Figure 6 (“CSF tau/aBeta,” “PET amyloid,” “multiple”); Figure S9 depicts all MTL models, with Bonferroni correction for 320 comparisons. In both figures, cross-sectional differences in predicted volumes at mean baseline age across subjects (73.5 years) are depicted instead of intercepts. Intercepts represent group differences at age zero (i.e., at birth) while we have measured and modeled cortical degeneration in older adults. The three MTL models in Figure 6 agree that there are significant cross-sectional disease-related differences in volumes across the cortex, with sparing of the sensorimotor and cingulate regions (Figure 6, top row). The three LME models, in contrast, detect a less widespread and less significant pattern of cross-sectional differences than the MTL models while “OLS” detects even fewer cross-sectional differences.

Longitudinally, the bottom row of Figure 6 shows both “Rand Int” and “Rand Int/Slp” have almost no significant slope differences in any region, while “Rand Int/Slp/Amyloid” detects some significant differences within parts of the temporal lobe, insula and parietal regions,

but does not detect the expected slope difference within the medial temporal lobe. The three MTL models, including “*PET amyloid*,” which represents the fairest comparison to the LME models, have significant differences across the temporal lobe (including the medial temporal lobe), insula, orbitofrontal region and, in the case of “*multiple*,” the lateral parietal region. Overall the MTL models infer a more plausible pattern of both cross-sectional and longitudinal disease effects than standard LME models.

It is reassuring that similar types of biological coupling (amyloid load measured via CSF and PET in “*CSF tau/aBeta*” and “*PET amyloid*” respectively) result in similar patterns of longitudinal differences. The longitudinal differences in the lateral parietal region detected by “*multiple*” may be due to its incorporation of all biomarker coupling priors: “*APOE*” and “*CSF ptau*” also show some differences within that region (Figure S9, bottom row). In contrast to these biomarker-coupled models, “*random*” does not detect any significant slope differences while “*OLS*” detects few cross-sectional differences; neither model is plausible given other studies of AD-related atrophy (Frisoni, Fox, Jack, Scheltens, & Thompson, 2010; Risacher et al., 2010; Ziegler et al., 2015).

Interestingly, “*plain*” only detects longitudinal differences within the medial temporal and temporal pole, suggesting that while this model can reliably detect strong true effects (see simulations), it may not be as sensitive as models with additional prior information. Further to this, Figure S10 depicts data for two regions: the medial temporal region, where most models agree that there are both cross-sectional and longitudinal differences, and the lateral temporal region, where “*plain*” detects no longitudinal differences, though they are clearly evident in the figure. We further observe that “*APOE*” detects a similar though weaker pattern of longitudinal differences compared to the other biomarker coupled models, suggesting that coupling based on similarity of genetic AD risk, conferred at birth, is less informative than coupling based on levels of amyloid accumulated decades later in older adults.

We also tested for cortical differences in subjects with differing numbers of APOE ϵ 4 alleles (either 0, 1, or 2), analyzing each diagnostic group separately. Figure S11 depicts group differences in number of alleles for “*APOE*,” “*PET amyloid*,” and “*multiple*.” “*OLS*,” “*plain*,” and “*random*” showed no differences in neither baseline volumes nor slopes (data not shown) while “*CSF ptau*” and “*CSF tau/aBeta*” (not shown) had spatial patterns resembling that of “*PET amyloid*,” which shows allele-related differences in temporo-parieto-frontal, insular and anterior cingulate regions within the MCI group. There is a more widespread pattern of slope differences in “*APOE*” and “*multiple*” which is consistent with Ziegler et al. (2015), who found slope differences within temporo-parieto-frontal cortical gray matter in stable MCI subjects. However, these models also find slope differences within the insula and anterior cingulate in MCI subjects that were not reported in that study.

4 | DISCUSSION

We have presented a multi-task learning based approach to modeling individuals' longitudinal biomarker trajectories, setting the learning of each trajectory as a “task” and using flexible covariance priors to

couple tasks (i.e., subjects) during model training. Thanks to its parametric Bayesian formulation, our approach makes probabilistic predictions, infers distributions over parameters and allows for the comparison of competing models via model evidence. Using empirical Bayes (rather than time-consuming cross-validation), we showed how we can combine (a) fully decoupled models (i.e., individual-specific trajectory models; OLS-like); (b) fully coupled models (i.e., a common trajectory across subjects; LME-like); and (c) models coupled via one or more biomarker-based similarity matrices (i.e., kernels). In this way, our approach uses multi-kernel learning and capitalizes on different aspects of biology measured by different biomarkers, within a multi-task learning framework.

We performed simulations of trajectories having group wise variations in intercept and slope, showing that even the simplest version of our proposed model (“*plain*,” mixing decoupled and fully coupled models) dramatically outperforms decoupled models (“*OLS*”) in terms of predictive accuracy. We achieved further reductions in prediction error by adding kernel-based coupling using both random information and biomarkers (in various configurations, with and without oracle-like knowledge of simulation scenario). Interestingly, random-information-based kernels performed almost as well as the biomarker-based kernels (Figure 2), though the biomarker-based models (“*Gaussian both*” and the oracle-like models of each scenario) had better inference of true group differences (Figure 3). As such, biomarker-based models are the better choice for accurately making predictions and inferring parameters. We further conclude that “*Gaussian both*,” which allows biomarker-based coupling in all parameter types (e.g., intercepts and slopes) is a better choice than “*linear both*” in terms of predictive performance and parameter inference. We emphasize the importance of parameter inference for both scientific (e.g., model interpretation) and translational purposes (e.g., trajectory parameter-based biomarkers such as ROI rates of change).

In this article, we used empirical Bayes to estimate the coupling and noise hyperparameters, leading to a point estimate of the prior values of these variables. However, the full Bayesian approach may better account for both parameter and predictive uncertainty by placing priors on hyperparameters and estimating their posterior distributions. In our simulations, the two approaches had similar prediction errors and coverages. The models differed more in their parameter estimates: full Bayes had better parameter coverage and lower parameter error in some cases. On the other hand, empirical Bayes' gradient descent based hyperparameter optimization runs significantly faster and scales better with the number of tasks than full Bayes' MCMC sampling, thus providing a critical advantage of EB over full Bayes in real world applications. It is important to note though that in cases where the necessary posteriors can be derived, Gibbs sampling can significantly reduce this computational burden, making full Bayes more appealing (see for example, Huertas et al., 2017).

We tested the assumption of independent measurement noise, parameterized by β in Equation (6), with additional simulations. In general, prediction and parameter estimation errors were similar to or lower than LME models across varying noise correlations (Figure S4). However, some degradation of parameter coverage was evident,

particularly at the highest noise correlation level, suggesting that a more general parameterization of the measurement error covariance (e.g., a block diagonal form allowing within-subject correlation) may be necessary in some situations. We also explored the effect of non-Gaussian distributed measurement error, finding that in general both the MTL and LME models were robust to error skewness in terms of both predictions and parameter estimates (Figure S5).

We applied the model to longitudinal data from the ADNI study, modeling trajectories of cortical ROIs across CN, MCI, and AD subjects using kernels formed from amyloid PET, CSF, and genetic (APOE) information. We showed degeneration throughout the cortex, with lateral regions degenerating faster than medial regions (Figure 4). We showed significantly decreased prediction errors due to coupling ("plain" vs. "OLS") and further decreases when adding kernel-based coupling, with a small difference between the random-information versus biomarker coupled models in some ROIs (Figures 4 and S7).

Our model offers improved interpretability and more concrete biological explanations of trajectory differences across diagnostic groups compared to the baseline models. Here, we were mainly interested in understanding how cortical degeneration varies across diagnostic groups, which required that we carefully interpret the patterns of group differences (Figures 6 and S9). Single biomarker models based on either "PET amyloid" or "CSF tau/aBeta" had cross-sectional and longitudinal group differences that were consistent with the literature and had the most evidence in their favor (Figure 5). Importantly, this analysis showed the benefit in coupling cortical trajectories based on baseline measures of amyloid deposition measured via PET or amyloid-to-tau ratio via CSF, which is consistent with the prevailing disease progression model of AD in which amyloid deposition precedes change in brain structure (Jack et al., 2010). Coupling based on genetic risk for AD as realized by the APOE genotype was inferior to using baseline amyloid-based biomarkers. This agrees with the literature in that APOE genotype is the genetic risk and amyloid biomarker levels represent the realization of that risk. Furthermore, we showed that combining multiple kernels is effective in the sense that "multiple," the multi-modal model, was as good as the best individual model in terms of model evidence and parameter inference. Thus, our approach removes the requirement to pre-select any specific biomarker.

All coupled models had significant diagnostic group differences across the cortex at mean baseline age, agreeing with the pattern of later-stage neurofibrillary changes due to AD that have been shown to be detectable via MRI (Braak & Braak, 1991; Whitwell et al., 2008), along with many of the AD discrimination studies that have used cross-sectional structural MRI based features (Arbabshirani, Plis, Sui, & Calhoun, 2016). In particular, the pattern of cross-sectional differences we find aligns with Karas et al., (Karas et al., 2003), which reported AD-related differences within the temporal lobe and insula, with sparing of the sensorimotor cortex. We also found no significant differences within the motor and sensory ROIs, supporting the idea that sensorimotor function is relatively spared in AD, unless the disease is very advanced (Ferreri et al., 2016; Suvà et al., 1999). Among the models with high model evidence in their favor, namely "CSF tau/aBeta," "PET amyloid," and "multiple," there were significant longitudinal (i.e., slope) differences within the temporal lobe, orbitofrontal

region, insula and lateral parietal region. These findings are similar to the patterns of group differences in 1 year atrophy depicted in Risacher et al. (2010), although the authors did not focus on their apparent findings within the insula. Insel et al. (2015) identified changes within the insula and temporal regions occurring prior to the clinical threshold for amyloid- β positivity, and interestingly, we detect longitudinal differences in these regions with models that couple based on similarity of protein measures.

In addition to clinical diagnosis, we also investigated the effect of APOE $\epsilon 4$, the major genetic risk factor for late-onset AD, analyzing differences in subjects grouped by number of $\epsilon 4$ alleles (Figure S11). We found no cross-sectional volume differences at mean baseline age within each group and few significant longitudinal differences within the CN and AD groups. The CN finding is consistent with the literature: Filippini et al. (2009) found no volumetric differences within the brain between young, healthy $\epsilon 4$ carriers and matched non-carriers using cross-sectional information while Raz et al. (2010) found no differences due to $\epsilon 4$ within healthy middle-aged and older adults using longitudinal data. Our findings indicate similar homogeneity within AD subjects. Within the MCI group we found a temporo-parietal-frontal pattern of slope differences that aligned with previous literature (Ziegler et al., 2015) along with additional slope differences with the insula and anterior cingulate. We note that the findings within this group may be due to both the larger sample size and greater heterogeneity of the MCI group compared to the CN and AD groups.

We also compared our novel MTL approach to a widely available LME implementation, showing that MTL makes very similar prediction errors on the held-out ADNI follow-ups (Figure S8). However, MTL detected more widespread cross-sectional group differences than the three LME models we considered and, importantly, more significant longitudinal differences within the temporal lobe (Figure 6). As such the MTL based parameters appear to be more plausible than the LME based parameters. Additionally, our method automatically finds the covariance structure that best explains the training data (within the limit of the chosen parameterization), removing modeling decisions such as whether a variable is or is not a random effect.

The approach we have presented has several limitations, however. Firstly, computing the log marginal likelihood at each optimization step involves the inversion of the prior covariance matrix (see Appendix), which scales cubically with the number of subjects in the worst case. This precludes coupling beyond hundreds of subjects and restricts us to univariate modeling. A multivariate approach would exacerbate the problem, scaling cubically with the product of subjects by variables. Reduced rank approaches or inducing point methods may speed up computation, as would a diagonal approximation of the matrix inversions, sacrificing accuracy for speed. Alternatively, one could use GPUs; Tensorflow has highly optimized linear algebra routines for matrix operations that can deliver an order of magnitude speed improvements (Abadi et al., 2016). Secondly, beyond computational considerations, our model may not capture long term, nonlinear trends that are only evident across subjects (see for example, Donohue et al., 2014). To properly model these may require adding a fixed effects component to accommodate higher-order polynomial functions

describing group-level trajectories. Alternatively, one may switch to modeling trajectories of study time, which may introduce significant intercept differences.

There are multiple directions for future work. As mentioned in the introduction, the method we present is not a disease progression model and as such it does not estimate a disease stage for each subject. It does, however, provide plausible estimates of trajectory parameters, which may serve as valuable inputs to a staging model. Future work will investigate the staging of subjects based on these parameters within an EBM (Young et al., 2014), providing insight into the role of brain structural changes during the progression from normal cognition to Alzheimer's disease (Jack et al., 2010). We can also extend our understanding of the relationship between genetics and cortical atrophy beyond APOE to all single nucleotide polymorphisms (SNPs) using multivariate methods such as partial least squares (PLS; Lorenzi et al., 2018) or canonical correlation analysis (Szefer, Lu, Nathoo, Beg, & Graham, 2017). Finally, we can generalize the approach to simultaneously model multiple variables across subjects (i.e., multi-output learning), where interesting modeling possibilities (coupling parameters across variables within and between subjects) and computational challenges abound. It is important to note that benefits of such an approach depend on whether there are strong multivariate relationships that can be modeled through either correlated parameters or errors. For example, Marinescu et al., (2019) show that there are widespread patterns in neurodegenerative disease progression that can be modeled via spatial coupling, while earlier studies showed only a modest benefit of this type of coupling relative to the computational effort involved (Marquand, Brammer, et al., 2014a; Marquand, Brammer, et al., 2014; Zhang & Shen, 2012).

ACKNOWLEDGMENTS

Authors are grateful to Dr. Marco Lorenzi and Prof. Jonathan Schott for their comments and suggestions. This project has received funding from the European Union's Horizon 2020 research and innovation program under grant agreement No. 666992. EPSRC grants M020533, M006093, J020990 additionally support DCA's work on this topic. Andre Altmann holds an MRC eMedLab Medical Bioinformatics Career Development Fellowship. This work was supported by the Medical Research Council [grant number MR/L016311/1]. Marzia Antonella Scelsi acknowledges financial support by the EPSRC-funded UCL Centre for Doctoral Training in Medical Imaging (EP/L016478/1). Andre Marquand gratefully acknowledges support from the Netherlands Organization for Scientific Research (NOW) via a Verniewingsimpuls VIDI fellowship (91716415). Sebastien Ourselin receives funding from the EPSRC (EP/H046410/1, EP/J020990/1, EP/K005278), the MRC (MR/J01107X/1), the EU-FP7 project VPH-DARE@IT (FP7-ICT-2011-9-601055), the NIHR Biomedical Research Unit (Dementia) at UCL and the National Institute for Health Research University College London Hospitals Biomedical Research Centre (NIHR BRC UCLH/UCL High Impact Initiative- BW.mn.BRC10269). Data collection and sharing for this project was funded by the Alzheimer's Disease Neuroimaging Initiative (ADNI) (National

Institutes of Health Grant U01 AG024904) and DOD ADNI (Department of Defense award number W81XWH-12-2-0012). ADNI is funded by the National Institute on Aging, the National Institute of Biomedical Imaging and Bioengineering, and through generous contributions from the following: Abbreviations: Alzheimer's Association; Alzheimer's Drug Discovery Foundation; Araclon Biotech; BioClinica, Inc.; Biogen; Bristol-Myers Squibb Company; CereSpir, Inc.; Cogstate; Eisai Inc.; Elan Pharmaceuticals, Inc.; Eli Lilly and Company; EuroImmun; F. Hoffmann-La Roche Ltd., and its affiliated company Genentech, Inc.; Fujirebio; GE Healthcare; IXICO Ltd.; Janssen Alzheimer Immunotherapy Research & Development, LLC.; Johnson & Johnson Pharmaceutical Research & Development LLC.; Lumosity; Lundbeck; Merck & Co., Inc.; Meso Scale Diagnostics, LLC.; NeuroRx Research; Neurotrack Technologies; Novartis Pharmaceuticals Corporation; Pfizer Inc.; Piramal Imaging; Servier; Takeda Pharmaceutical Company; and Transition Therapeutics. The Canadian Institutes of Health Research is providing funds to support ADNI clinical sites in Canada. Private sector contributions are facilitated by the Foundation for the National Institutes of Health (www.fnih.org). The grantee organization is the Northern California Institute for Research and Education, and the study is coordinated by the Alzheimer's Therapeutic Research Institute at the University of Southern California. ADNI data are disseminated by the Laboratory for Neuro Imaging at the University of Southern California.

ORCID

Leon M. Aksman  <https://orcid.org/0000-0003-2342-0780>

REFERENCES

- Abadi, M., Barham, P., Chen, J., Chen, Z., Davis, A., Dean, J., Devin, M., Ghemawat, S., Irving, G., Isard, M., Kudlur, M., Levenberg, J., Monga, R., Moore, S., Murray, D.G., Steiner, B., Tucker, P., Vasudevan, V., Warden, P., Wicke, M., Yu, Y., Zheng, X., 2016. TensorFlow: A system for large-scale machine learning.
- Arbabshirani, M. R., Plis, S., Sui, J., & Calhoun, V. D. (2016). Single subject prediction of brain disorders in neuroimaging: Promises and pitfalls. *NeuroImage*, 145, 137–165. <https://doi.org/10.1016/j.neuroimage.2016.02.079>
- Bernal-Rusiel, J. L., Greve, D. N., Reuter, M., Fischl, B., Sabuncu, M. R., & Alzheimer's Disease Neuroimaging Initiative. (2013). Statistical analysis of longitudinal neuroimage data with linear mixed effects models. *NeuroImage*, 66, 249–260. <https://doi.org/10.1016/j.neuroimage.2012.10.065>
- Bernal-Rusiel, J. L., Reuter, M., Greve, D. N., Fischl, B., & Sabuncu, M. R. (2013). Spatiotemporal linear mixed effects modeling for the mass-univariate analysis of longitudinal neuroimage data. *NeuroImage*, 81, 358–370. <https://doi.org/10.1016/j.neuroimage.2013.05.049>
- Bishop, C. M. (2007). *Pattern recognition and machine learning*. New York: Springer.
- Bonilla, E. V., Chai, K. M. A., & Williams, C. K. I. (2008). Multi-task Gaussian process prediction. *Advances in Neural Information Processing Systems*, 20, 153–160.
- Braak, H., & Braak, E. (1991). Neuropathological staging of Alzheimer-related changes. *Acta Neuropathologica (Berl.)*, 82, 239–259. <https://doi.org/10.1007/BF00308809>

- Buckner, R. L., Snyder, A. Z., Shannon, B. J., LaRossa, G., Sachs, R., Fotenos, A. F., ... Mintun, M. A. (2005). Molecular, structural, and functional characterization of Alzheimer's disease: Evidence for a relationship between default activity, amyloid, and memory. *The Journal of Neuroscience*, *25*, 7709–7717. <https://doi.org/10.1523/JNEUROSCI.2177-05.2005>
- Cardoso, M. J., Modat, M., Wolz, R., Melbourne, A., Cash, D., Rueckert, D., & Ourselin, S. (2015). Geodesic information flows: Spatially-variant graphs and their application to segmentation and fusion. *IEEE Transactions on Medical Imaging*, *34*, 1976–1988. <https://doi.org/10.1109/TMI.2015.2418298>
- Carpenter, B., Gelman, A., Hoffman, M. D., Lee, D., Goodrich, B., Betancourt, M., ... Riddell, A. (2017). Stan: A probabilistic programming language. *Journal of Statistical Software*, *76*, 1–32. <https://doi.org/10.18637/jss.v076.i01>
- Curran, P. J., Obeidat, K., & Losardo, D. (2010). Twelve frequently asked questions about growth curve modeling. *Journal of Cognition and Development*, *11*, 121–136. <https://doi.org/10.1080/15248371003699969>
- Donohue, M. C., Jacqmin-Gadda, H., Le Goff, M., Thomas, R. G., Raman, R., Gamst, A. C., ... Aisen, P. S. (2014). Estimating long-term multivariate progression from short-term data. *Alzheimer's & Dementia*, *10*, S400–S410. <https://doi.org/10.1016/j.jalz.2013.10.003>
- Ferreri, F., Vecchio, F., Vollero, L., Guerra, A., Petrichella, S., Ponzio, D., ... Di Lazzaro, V. (2016). Sensorimotor cortex excitability and connectivity in Alzheimer's disease: A TMS-EEG co-registration study. *Human Brain Mapping*, *37*, 2083–2096. <https://doi.org/10.1002/hbm.23158>
- Filippini, N., MacIntosh, B. J., Hough, M. G., Goodwin, G. M., Frisoni, G. B., Smith, S. M., ... Mackay, C. E. (2009). Distinct patterns of brain activity in young carriers of the APOE-ε4 allele. *Proceedings of the National Academy of Sciences of the United States of America*, *106*, 7209–7214. <https://doi.org/10.1073/pnas.0811879106>
- Fitzmaurice, G. M., Laird, N. M., & Ware, J. H. (2011). *Applied longitudinal analysis*. Hoboken, New Jersey: Wiley.
- Fonteyn, H. M., Modat, M., Clarkson, M. J., Barnes, J., Lehmann, M., Hobbs, N. Z., ... Alexander, D. C. (2012). An event-based model for disease progression and its application in familial Alzheimer's disease and Huntington's disease. *NeuroImage*, *60*, 1880–1889. <https://doi.org/10.1016/j.neuroimage.2012.01.062>
- Freeborough, P. A., & Fox, N. C. (1997). The boundary shift integral: An accurate and robust measure of cerebral volume changes from registered repeat MRI. *IEEE Transactions on Medical Imaging*, *16*, 623–629. <https://doi.org/10.1109/42.640753>
- Frisoni, G. B., Fox, N. C., Jack, C. R., Scheltens, P., & Thompson, P. M. (2010). The clinical use of structural MRI in Alzheimer disease. *Nature Reviews. Neurology*, *6*, 67–77. <https://doi.org/10.1038/nrneuro.2009.215>
- Gelman, A., Carlin, J. B., Stern, H. S., Dunson, D. B., Vehtari, A., & Rubin, D. B. (2013). *Bayesian data analysis, third edition* (3rd ed.). Boca Raton: Chapman and Hall/CRC.
- Greenlaw, K., Szefer, E., Graham, J., Lesperance, M., & Nathoo, F. S. (2017). A Bayesian group sparse multi-task regression model for imaging genetics. *Bioinformatics*, *33*, 2513–2522. <https://doi.org/10.1093/bioinformatics/btx215>
- Guillaume, B., Hua, X., Thompson, P. M., Waldorp, L., & Nichols, T. E. (2014). Fast and accurate modelling of longitudinal and repeated measures neuroimaging data. *NeuroImage*, *94*, 287–302. <https://doi.org/10.1016/j.neuroimage.2014.03.029>
- Hempel, H., Blennow, K., Shaw, L. M., Hoessler, Y. C., Zetterberg, H., & Trojanowski, J. Q. (2010). Total and phosphorylated tau protein as biological markers of Alzheimer's disease. *Experimental Gerontology*, *45*, 30–40. <https://doi.org/10.1016/j.exger.2009.10.010>
- Harold, D., Abraham, R., Hollingworth, P., Sims, R., Gerrish, A., Hamshere, M., ... Williams, J. (2009). Genome-wide association study identifies variants at CLU and PICALM associated with Alzheimer's disease, and shows evidence for additional susceptibility genes. *Nature Genetics*, *41*, 1088–1093. <https://doi.org/10.1038/ng.440>
- Hinrichs, C., Singh, V., Xu, G., & Johnson, S. C. (2011). Predictive markers for AD in a multi-modality framework: An analysis of MCI progression in the ADNI population. *NeuroImage*, *55*, 574–589. <https://doi.org/10.1016/j.neuroimage.2010.10.081>
- Huertas, I., Oldehinkel, M., van Oort, E. S. B., Garcia-Solis, D., Mir, P., Beckmann, C. F., & Marquand, A. F. (2017). A Bayesian spatial model for neuroimaging data based on biologically informed basis functions. *NeuroImage*, *161*, 134–148. <https://doi.org/10.1016/j.neuroimage.2017.08.009>
- Insel, P. S., Mattsson, N., Donohue, M. C., Mackin, R. S., Aisen, P. S., Jack, C. R., ... Weiner, M. W. (2015). The transitional association between β-amyloid pathology and regional brain atrophy. *Alzheimer's & Dementia*, *11*, 1171–1179. <https://doi.org/10.1016/j.jalz.2014.11.002>
- Jack, C. R., Knopman, D. S., Jagust, W. J., Shaw, L. M., Aisen, P. S., Weiner, M. W., ... Trojanowski, J. Q. (2010). Hypothetical model of dynamic biomarkers of the Alzheimer's pathological cascade. *Lancet Neurology*, *9*, 119–128. [https://doi.org/10.1016/S1474-4422\(09\)70299-6](https://doi.org/10.1016/S1474-4422(09)70299-6)
- Jedynak, B. M., Lang, A., Liu, B., Katz, E., Zhang, Y., Wyman, B. T., ... Prince, J. L. (2012). A computational neurodegenerative disease progression score: Method and results with the Alzheimer's disease neuroimaging initiative cohort. *NeuroImage*, *63*, 1478–1486. <https://doi.org/10.1016/j.neuroimage.2012.07.059>
- Karas, G. B., Burton, E. J., Rombouts, S. A., van Schijndel, R. A., O'Brien, J. T., Scheltens, P. h., ... Barkhof, F. (2003). A comprehensive study of gray matter loss in patients with Alzheimer's disease using optimized voxel-based morphometry. *NeuroImage*, *18*, 895–907.
- Kwee, L. C., Liu, D., Lin, X., Ghosh, D., & Epstein, M. P. (2008). A powerful and flexible multilocus association test for quantitative traits. *American Journal of Human Genetics*, *82*, 386–397. <https://doi.org/10.1016/j.ajhg.2007.10.010>
- Laird, N. M., & Ware, J. H. (1982). Random-effects models for longitudinal data. *Biometrics*, *38*, 963–974.
- Landau, S. M., Fero, A., Baker, S. L., Koeppe, R., Mintun, M., Chen, K., ... Jagust, W. J. (2015). Measurement of longitudinal β-amyloid change with 18F-florbetapir PET and standardized uptake value ratios. *Journal of Nuclear Medicine*, *56*, 567–574. <https://doi.org/10.2967/jnumed.114.148981>
- Liu, C.-C., Kanekiyo, T., Xu, H., & Bu, G. (2013). Apolipoprotein E and Alzheimer disease: Risk, mechanisms and therapy. *Nature Reviews. Neurology*, *9*, 106–118. <https://doi.org/10.1038/nrneuro.2012.263>
- Lorenzi, M., Altmann, A., Gutman, B., Wray, S., Arber, C., Hibar, D. P., ... Initiative, for the A.D.N. (2018). Susceptibility of brain atrophy to TRIB3 in Alzheimer's disease, evidence from functional prioritization in imaging genetics. *Proceedings of the National Academy of Sciences*, *12*, 3162–3167. <https://doi.org/10.1073/pnas.1706100115>
- Lorenzi, M., Filippone, M., Frisoni, G. B., Alexander, D. C., Ourselin, S., & Alzheimer's Disease Neuroimaging Initiative. (2017). Probabilistic disease progression modeling to characterize diagnostic uncertainty: Application to staging and prediction in Alzheimer's disease. *NeuroImage*, *190*, 56–68. <https://doi.org/10.1016/j.neuroimage.2017.08.059>
- Lorenzi, M., Ziegler, G., Alexander, D. C., & Ourselin, S. (2015). Efficient Gaussian process-based Modelling and prediction of image time series. *Information Processing in Medical Imaging*, *24*, 626–637.
- Marinescu, R. V., Eshaghi, A., Lorenzi, M., Young, A. L., Oxtoby, N. P., Garbarino, S., ... Alexander, D. C. (2019). DIVE: A spatiotemporal progression model of brain pathology in neurodegenerative disorders. *NeuroImage*, *192*, 166–177. <https://doi.org/10.1016/j.neuroimage.2019.02.053>
- Marquand, A. F., Williams, S.C.R., Doyle, O.M., Rosa, M.J., 2014. Full Bayesian multi-task learning for multi-output brain decoding and accommodating missing data. Presented at the 2014 International Workshop on Pattern Recognition in Neuroimaging, pp. 1–4. <https://doi.org/10.1109/PRNI.2014.6858533>

- Marquand, A. F., Brammer, M., Williams, S. C. R., & Doyle, O. M. (2014). Bayesian multi-task learning for decoding multi-subject neuroimaging data. *NeuroImage*, 92, 298–311. <https://doi.org/10.1016/j.neuroimage.2014.02.008>
- Nathoo, F.S., Greenlaw, K., Lesperance, M., 2016. Regularization parameter selection for a bayesian group sparse multi-task regression model with application to imaging genomics, in: Presented at the 2016 International Workshop on Pattern Recognition in Neuroimaging (PRNI), pp. 1–4. <https://doi.org/10.1109/PRNI.2016.7552328>
- Oxtoby, N. P., & Alexander, D. C. (2017). Imaging plus X: Multimodal models of neurodegenerative disease. *Current Opinion in Neurology*, 30, 371–379. <https://doi.org/10.1097/WCO.0000000000000460>
- Penny, W. D. (2012). Comparing dynamic causal models using AIC, BIC and free energy. *NeuroImage, Neuroergonomics: The Human Brain in Action and at Work*, 59, 319–330. <https://doi.org/10.1016/j.neuroimage.2011.07.039>
- Penny, W. D., Stephan, K. E., Mechelli, A., & Friston, K. J. (2004). Comparing dynamic causal models. *NeuroImage*, 22, 1157–1172. <https://doi.org/10.1016/j.neuroimage.2004.03.026>
- Rasmussen, C. E. (2006). *Gaussian processes for machine learning*. Cambridge, MA: MIT Press.
- Rasmussen, C. E., & Nickisch, H. (2010). Gaussian processes for machine learning (GPML) toolbox. *Journal of Machine Learning Research*, 11, 3011–3015.
- Raz, N., Ghisletta, P., Rodrigue, K. M., Kennedy, K. M., & Lindenberger, U. (2010). Trajectories of brain aging in middle-aged and older adults: Regional and individual differences. *NeuroImage*, 51, 501–511. <https://doi.org/10.1016/j.neuroimage.2010.03.020>
- Risacher, S. L., Shen, L., West, J. D., Kim, S., McDonald, B. C., Beckett, L. A., ... Saykin, A. J. (2010). Longitudinal MRI atrophy biomarkers: Relationship to conversion in the ADNI cohort. *Neurobiology of Aging*, 31, 1401–1418. <https://doi.org/10.1016/j.neurobiolaging.2010.04.029>
- Scelsi, M., Khan, R. R., Lorenzi, M., Christopher, L., Greicius, M., Schott, J., ... Altmann, A. (2018). Genetic study of multimodal imaging Alzheimer's disease progression score implicates novel loci. *Brain*, 141, 2167–2180.
- Schiratti, J.-B., Allasonnière, S., Colliot, O., & Durrleman, S. (2017). A Bayesian mixed-effects model to learn trajectories of changes from repeated manifold-valued observations. *Journal of Machine Learning Research*, 18, 1–33.
- Smith, S. M., De Stefano, N., Jenkinson, M., & Matthews, P. M. (2001). Normalized accurate measurement of longitudinal brain change. *Journal of Computer Assisted Tomography*, 25, 466–475.
- Sunderland, T., Linker, G., Mirza, N., Putnam, K. T., Friedman, D. L., Kimmel, L. H., ... Cohen, R. M. (2003). Decreased beta-amyloid1-42 and increased tau levels in cerebrospinal fluid of patients with Alzheimer disease. *JAMA*, 289, 2094–2103. <https://doi.org/10.1001/jama.289.16.2094>
- Suvà, D., Favre, I., Kraftsik, R., Esteban, M., Lobrinus, A., & Miklossy, J. (1999). Primary motor cortex involvement in Alzheimer disease. *Journal of Neuropathology and Experimental Neurology*, 58, 1125–1134.
- Szefer, E., Lu, D., Nathoo, F., Beg, M. F., & Graham, J. (2017). Multivariate association between single-nucleotide polymorphisms in Alzgene linkage regions and structural changes in the brain: Discovery, refinement and validation. *Statistical Applications in Genetics and Molecular Biology*, 16, 367–386. <https://doi.org/10.1515/sagmb-2016-0077>
- Telzer, E. H., McCormick, E. M., Peters, S., Cosme, D., Pfeifer, J. H., & van Duijvenvoorde, A. C. K. (2018). Methodological considerations for developmental longitudinal fMRI research. *Developmental Cognitive Neuroscience*, 33, 149–160. <https://doi.org/10.1016/j.dcn.2018.02.004>
- Whitwell, J. L., Josephs, K. A., Murray, M. E., Kantarci, K., Przybelski, S. A., Weigand, S. D., ... Jack, C. R. (2008). MRI correlates of neurofibrillary tangle pathology at autopsy. *Neurology*, 71, 743–749. <https://doi.org/10.1212/01.wnl.0000324924.91351.7d>
- Woolrich, M.W., 2012. Bayesian inference in FMRI. *NeuroImage, 20 YEARS OF fMRI* 62, 801–810. <https://doi.org/10.1016/j.neuroimage.2011.10.047>
- Young, A. L., Oxtoby, N. P., Daga, P., Cash, D. M., Fox, N. C., Ourselin, S., ... Alexander, D. C. (2014). A data-driven model of biomarker changes in sporadic Alzheimer's disease. *Brain*, 137, 2564–2577. <https://doi.org/10.1093/brain/awu176>
- Young, J., Modat, M., Cardoso, M. J., Mendelson, A., Cash, D., & Ourselin, S. (2013). Accurate multimodal probabilistic prediction of conversion to Alzheimer's disease in patients with mild cognitive impairment. *NeuroImage: Clinical*, 2, 735–745. <https://doi.org/10.1016/j.nicl.2013.05.004>
- Zhang, D., & Shen, D. (2012). Multi-modal multi-task learning for joint prediction of multiple regression and classification variables in Alzheimer's disease. *NeuroImage*, 59, 895–907. <https://doi.org/10.1016/j.neuroimage.2011.09.069>
- Zhang, D., Wang, Y., Zhou, L., Yuan, H., & Shen, D. (2011). Multimodal classification of Alzheimer's disease and mild cognitive impairment. *NeuroImage*, 55, 856–867. <https://doi.org/10.1016/j.neuroimage.2011.01.008>
- Ziegler, G., Penny, W. D., Ridgway, G. R., Ourselin, S., & Friston, K. J. (2015). Estimating anatomical trajectories with Bayesian mixed-effects modeling. *NeuroImage*, 121, 51–68. <https://doi.org/10.1016/j.neuroimage.2015.06.094>

SUPPORTING INFORMATION

Additional supporting information may be found online in the Supporting Information section at the end of this article.

How to cite this article: Aksman LM, Scelsi MA, Marquand AF, Alexander DC, Ourselin S, Altmann A, for ADNI. Modeling longitudinal imaging biomarkers with parametric Bayesian multi-task learning. *Hum Brain Mapp.* 2019;40:3982–4000. <https://doi.org/10.1002/hbm.24682>

APPENDIX

We wish to find the hyperparameters that maximize the model's marginal likelihood. For computational and analytic reasons, it is easier to minimize the negative (natural) log marginal likelihood, setting this as the optimizer's objective. We need the partial derivatives with respect to each hyperparameter, constraining each to be strictly positive. For the noise term β this is a natural constraint; for the coupling weights α we follow the rule that a positive sum of valid kernels is also a valid kernel. To impose these constraints within an unconstrained optimizer we transform the variables, optimizing $\log(\beta)$ and $\log(\alpha)$, which will be strictly positive when exponentiated. To derive the necessary partial derivatives with respect to the transformed variables we make use of the chain rule:

$$\begin{aligned} \frac{\partial \log(\mathbf{y}|\boldsymbol{\alpha}, \beta)}{\partial \log(\beta)} &= \frac{\partial \log(\mathbf{y}|\boldsymbol{\alpha}, \beta)}{\partial \beta} \frac{\partial \beta}{\partial \log(\beta)} = \frac{\partial \log(\mathbf{y}|\boldsymbol{\alpha}, \beta)}{\partial \beta} \beta \\ &= \frac{m}{2} - \frac{\beta}{2} \mathbf{y}^T \mathbf{y} + \beta \mathbf{y}^T \mathbf{X} \mathbf{m} + \beta^2 \mathbf{y}^T \mathbf{X} \mathbf{b} - \frac{\beta}{2} \mathbf{m}^T \mathbf{X}^T \mathbf{X} \mathbf{m} - \beta^2 \mathbf{b}^T \mathbf{X}^T \mathbf{X} \mathbf{m} \\ &\quad - \beta \mathbf{b}^T \boldsymbol{\Sigma}(\boldsymbol{\alpha})_{\text{prior}}^{-1} \mathbf{m} - \frac{\beta}{2} \text{tr}(\mathbf{A}^{-1} \mathbf{X}^T \mathbf{X}) \\ \frac{\partial \log(\mathbf{y}|\boldsymbol{\alpha}, \beta)}{\partial \log(\alpha_i)} &= \frac{\partial \log(\mathbf{y}|\boldsymbol{\alpha}, \beta)}{\partial \alpha_i} \frac{\partial \alpha_i}{\partial \log(\alpha_i)} = \frac{\partial \log(\mathbf{y}|\boldsymbol{\alpha}, \beta)}{\partial \alpha_i} \alpha_i \end{aligned}$$

where α_i is an element within vector $\boldsymbol{\alpha}$, $\mathbf{b} = (\mathbf{I}_{nd} - \beta \mathbf{A}^{-1} \mathbf{X}^T \mathbf{X}) \mathbf{A}^{-1} \mathbf{X}^T \mathbf{y}$ and

$$\begin{aligned} \frac{\partial \log(\mathbf{y}|\boldsymbol{\alpha}, \beta)}{\partial \alpha_i} &= -\frac{1}{2} \text{tr} \left(\boldsymbol{\Sigma}(\boldsymbol{\alpha})_{\text{prior}}^{-1} \frac{\partial \boldsymbol{\Sigma}(\boldsymbol{\alpha})_{\text{prior}}}{\partial \alpha_i} \right) - \frac{1}{2} \text{tr}(\mathbf{A}^{-1} \mathbf{F}) \\ &\quad + \beta \mathbf{y}^T \mathbf{X} \mathbf{c} - \beta \mathbf{c}^T \mathbf{X}^T \mathbf{X} \mathbf{m} - \mathbf{c}^T \boldsymbol{\Sigma}(\boldsymbol{\alpha})_{\text{prior}}^{-1} \mathbf{m} - \frac{1}{2} \mathbf{m}^T \mathbf{F} \mathbf{m} \end{aligned}$$

$$\mathbf{F} = \frac{\partial \boldsymbol{\Sigma}(\boldsymbol{\alpha})_{\text{prior}}^{-1}}{\partial \alpha_i} = -\boldsymbol{\Sigma}(\boldsymbol{\alpha})_{\text{prior}}^{-1} \frac{\partial \boldsymbol{\Sigma}(\boldsymbol{\alpha})_{\text{prior}}}{\partial \alpha_i} \boldsymbol{\Sigma}(\boldsymbol{\alpha})_{\text{prior}}^{-1}$$

$$\mathbf{c} = -\beta \mathbf{A}^{-1} \mathbf{F} \mathbf{A}^{-1} \mathbf{X}^T \mathbf{y}$$

and the $\partial \boldsymbol{\Sigma}(\boldsymbol{\alpha})_{\text{prior}} / \partial \alpha_i$ depends on the α_i in question. We can easily change the parameterization of $\boldsymbol{\Sigma}(\boldsymbol{\alpha})_{\text{prior}}$ without breaking these equations, provided it remains invertible and differentiable with respect to its parameters.

For the form used in Equations (3)–(5), we need $\partial \boldsymbol{\Sigma}(\boldsymbol{\alpha})_{\text{prior}} / \partial \alpha_1 = \mathbf{I}_{nd}$, $\partial \boldsymbol{\Sigma}(\boldsymbol{\alpha})_{\text{prior}} / \partial \alpha_{i1} = \mathbf{I}_n \otimes \mathbf{M}_{ii}$, $\partial \boldsymbol{\Sigma}(\boldsymbol{\alpha})_{\text{prior}} / \partial \alpha_{i2} = \mathbf{1}_n \otimes \mathbf{M}_{ii}$ and $\partial \boldsymbol{\Sigma}(\boldsymbol{\alpha})_{\text{prior}} / \partial \alpha_{ij+2} = \mathbf{K}_j \otimes \mathbf{M}_{ii}$ for the matrix weighting hyperparameters, where $i = 1, \dots, d$ and $j = 1, \dots, k$. Some kernels may also have internal hyperparameters (also included in $\boldsymbol{\alpha}$); one such example is the σ_{SE} parameter of the SE kernel. In this case, we need $\partial \boldsymbol{\Sigma}(\boldsymbol{\alpha})_{\text{prior}} / \partial \sigma_{\text{SE}} = -\alpha_{ij+2} (\mathbf{D} \odot \mathbf{K}_j) \otimes \mathbf{M}_{ii}$ where $\mathbf{K}_j = \exp(-\sigma_{\text{SE}} \mathbf{D})$ and \odot is the element-wise product.